

# How flexibility induces streamlining in a two-dimensional flow

Silas Alben<sup>a)</sup> and Michael Shelley

*Applied Mathematics Laboratory, Courant Institute of Mathematical Sciences, New York University, New York, New York 10012*

Jun Zhang

*Department of Physics, Applied Mathematics Laboratory, Courant Institute of Mathematical Sciences, New York University, New York, New York 10012*

(Received 3 June 2003; accepted 5 December 2003; published online 8 April 2004)

Recent work in bio-fluid dynamics has studied the relation of fluid drag to flow speed for flexible organic structures, such as tree leaves, seaweed, and coral beds, and found a reduction in drag growth due to body reconfiguration with increasing flow speed. Our theoretical and experimental work isolates the role of elastic bending in this process. Using a flexible glass fiber wetted into a vertical soap-film flow, we identify a transition in flow speed beyond which fluid forces dominate the elastic response, and yield large deformations of the fiber that greatly reduce drag. We construct free-streamline models that couple fluid and elastic forces and solve them in an efficient numerical scheme. Shape self-similarity emerges, with a scaling set by the balance of forces in a small “tip region” about the flow’s stagnation point. The result is a transition from the classical  $U^2$  drag scaling of rigid bodies to a new  $U^{4/3}$  drag law. We derive an asymptotic expansion for the fiber shape and flow, based on the length-scale of similarity. This analysis predicts that the fiber and wake are quasiparabolic at large velocities, and obtains the new drag law in terms of the drag on the tip region. Under variations of the model suggested by the experiment—the addition of flow tunnel walls, and a back pressure in the wake—the drag law persists, with a simple modification. © 2004 American Institute of Physics. [DOI: 10.1063/1.1668671]

## I. INTRODUCTION

The need to withstand large fluid forces is common among sessile organisms, and serves as an important organizing principle for understanding their morphology. For example, the shape and length of seaweed plants have been shown to vary in accordance with the range of flow speeds experienced in coastal waves.<sup>1</sup> A tree’s roots, trunk, branches, stems, and leaves can be considered a compound biomechanical structure built to a criterion of size and stiffness determined by local wind conditions.<sup>2</sup> In recent work, Vogel has studied the drag and shape reconfiguration of leaves in typical wind speeds (up to 20 m/s). Rather than a rigid-body  $U^2$ -drag law, the drag grew more slowly as the leaves rolled up into conical shapes that tightened with increased wind speed.<sup>3</sup> In general, the reconfiguration due to stretching, twisting, and bending allows a reduction in drag compared with that on a rigid body in the original configuration for two main reasons: (i) the profile area presented to the flow becomes smaller, and (ii) the body assumes a more streamlined shape, which decreases fluid pressure forces for a given profile area.

These biological studies are becoming more quantitative, sometimes involving measurements of elastic moduli of organic materials and using simple models to understand their behavior in fluid flows. The current models of which we are aware<sup>4,5</sup> capture only the response of the body to a predeter-

mined fluid flow, ignoring the change in the flow itself due to body reconfiguration. Thus the fluid dynamics of the interaction is limited to the  $U^2$  drag law, possibly modulated by an empirical profile-width factor. This limitation is understandable. As intricate as the mechanical structure of a single tree leaf may be, the flow structure it induces as it folds up in the wind is still more complicated.

Although drag reduction due to flexibility is the focus of this work, the interaction of organisms’ flexible structures with the fluids they inhabit serves purposes beyond mere endurance. Activities such as feeding and locomotion depend upon the creation of specific flow patterns around a moving and deforming body.<sup>3</sup> An understanding of the simple flow-body interaction in this work is useful as a preliminary step to studying more complicated flows around flexible bodies. Previous work has studied such flow-body interactions in terms of manmade objects, such as flags,<sup>6,7</sup> parachutes,<sup>8</sup> and sails.<sup>9,10</sup>

Here we examine experimentally and theoretically the interaction of a high-speed two-dimensional fluid flow with a flexible surface—a “1D leaf in a 2D wind.” Experimentally, this flow is realized using a flexible glass fiber wetted into and held against a flowing soap film. Soap film is a convenient experimental system described by two-dimensional hydrodynamics in many aspects.<sup>6,11–14</sup> Our experimental setup allows us to simultaneously measure the flow velocity, observe the resultant fiber shape and flow structures, especially the wake, and to measure the fluid drag on the fiber. We identify a transition in a dimensionless flow speed beyond

<sup>a)</sup>Electronic mail: albens@cims.nyu.edu

which fluid forces dominate the fiber's elastic restoring forces, yielding large shape deformations and greatly reduced fluid drag. This is described in Sec. II.

The relative simplicity of this high-Reynolds-number flow makes it amenable to fluid dynamical modeling. Our model considers the interaction of the fiber, taken to be an inextensible, elastic beam, with free-streamline flows. This captures several main elements of the flow-fiber system: the deformation of the fiber by flow forces, the rearrangement of the flow by fiber deformation, and the effect of a nearly stagnant wake behind the bent fiber.

Free streamline theory was originated by Helmholtz<sup>15</sup> and Kirchhoff<sup>16</sup> to describe wake flows behind flat plates. Here we outline the aspects relevant to our model, which is described in Sec. III. The flow field is taken as incompressible and irrotational outside of a stagnant wake, which has a constant pressure equal to that at infinity. This is also the pressure on the free streamlines which separate from the body and enclose the wake. Methods of complex variables are used to determine the location of the free streamlines and the flow field for an obstacle whose shape is known. Some analytical properties of free-streamline flows, including results on existence and uniqueness for a variety of body and free-streamline geometries, are reviewed in Birkhoff *et al.*<sup>17</sup>

In reality, the wake flow is characterized by significant vorticity and turbulence, arising in part from the instability of the free shear layers that the free streamlines are intended to model. However, the time-averaged flow and pressure fields can have a relatively simple structure,<sup>18</sup> and good agreement with experiment has been found in modifications of the infinite-wake (Helmholtz) model which assume a constant wake pressure lower than that at infinity.<sup>19</sup> Two other simple and widely-studied wake models are the constant-vorticity Prandtl–Batchelor model,<sup>20</sup> and the wake-source model of Parkinson and Jandali.<sup>21</sup> The latter has also achieved good agreement with experiment, as far as the pressure distribution on the body. However, the Helmholtz wake is a plausible candidate for the asymptotic limit of the laminar wake flow as the body-scale Reynolds number  $Re \rightarrow \infty$ , and is consequently used in preference to the other two as a basis for theories incorporating the triple-deck theory of boundary-layer separation.<sup>22,23</sup> Thus the free streamline model remains widely used for separated, high-Re flows, which are difficult to analyze by other means.

In Sec. IV we analyze numerical solutions of our model. There are three striking features: (i) a transition velocity below which the drag shows a rigid-body  $U^2$  drag scaling, and above which the fiber shows large deformations and a much reduced drag growth; (ii) a new, much-reduced drag scaling of  $U^{4/3}$ , asymptotically beyond this transition; (iii) the emergence of self-similar fiber shapes, based on an intrinsic length scaling as  $U^{-2/3}$ . This is the length scale of the sharply-bent “tip region” of the fiber. These results suggest that the drag scaling is the product of the  $U^2$  pressure scaling and the  $U^{-2/3}$  length-scale over which it acts. This length scale decreases more rapidly than the profile width, which is the relevant length for rigid-body drag. Here the profile width decreases only as  $U^{-1/3}$ , as shown in Sec. V. We compare the fiber shapes and drag data with those of the experi-

ment, and find good agreement when a constant multiplicative shift in nondimensional flow velocity is assumed. This shift arises naturally when we vary the wake pressure in our model, as discussed below.

In Sec. V we derive several mathematical properties of the solutions, including those seen in the numerics, through an asymptotic analysis. First, we obtain an expansion for the drag when  $U$  is small, which is a regular perturbation of the flat-plate solution. Then we consider large  $U$ , and obtain the  $U^{-2/3}$  length-scale of similarity from the force balance. Using rescaled equations, we show that the dominance of the tip region implies that the universal fiber shape is quasiparabolic, and that the free streamlines asymptote to the same parabola. We then determine the magnitude of the first correction to the universal shape, and also find that it has an oscillatory form, with a characteristic wavelength that scales with the bending length. Using the form of the universal solution and that of the first correction, we show how the  $U^{4/3}$  drag scaling arises from the dominant tip-region contribution.

With a detailed understanding of the basic model, Sec. VI revisits discrepancies in the comparison of model and experiment in Sec. IV, in terms of the wake pressure. The wake is the variable part of the free-streamline model. Since the wake flow involves the complicated interaction of vorticity in the presence of turbulence, the theory is incomplete. There is not yet a consensus on how to predict the most basic aspects of the wake in steady flows past a flat plate or cylinder, such as its size and pressure distribution; some approaches are reviewed by Tanner.<sup>24</sup> One empirical fact is that the pressure in the near wake, that region within a body length of the body itself, is nearly constant for a given flow, and equal to that on the separated streamlines alongside the near wake. This is because the near-wake flow is practically stagnant. Knowledge of this constant is then sufficient to determine the pressure drag on the body, given the pressure distribution on the front face from the inviscid flow theory. Hence a number of free-streamline models have been developed to incorporate this constant pressure, normalized by the dynamic pressure, as a free parameter.<sup>25</sup>

Since experiments are conducted in finite flow tunnels, another important issue in these studies is the effect of the tunnel walls on the flow. Even distant walls cause a decreased wake pressure, resulting in a significant increase in drag over the unbounded case in flow models.<sup>26</sup>

Section VI considers the effects of walls and wake pressure through three related models, based on the Helmholtz model. The first model adds symmetrically-spaced flow-tunnel walls, which are seen to dramatically increase the fluid loading on the fiber. The second uses a finite Riabouchinsky mirror-image wake<sup>27</sup> in an unbounded flow, which allows direct variation of the wake-pressure. The third combines the effects of walls and variable wake pressure, and is readily understood in view of the first two. The main result of these additional models are that the  $U^{4/3}$  drag law persists, except that  $U$  is now the velocity on the free streamline of the fiber, different in general from that at infinity upstream. This implies the same drag scaling with respect to the velocity upstream when the wake pressure coefficient tends to a

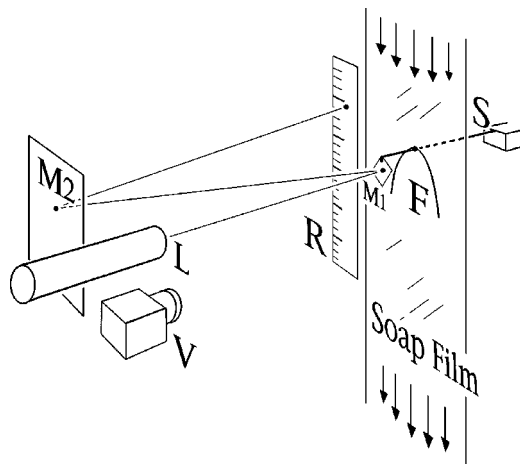


FIG. 1. The layout of the experiment. A glass fiber (F) is inserted into a flowing soap-film tunnel (partly shown). The fiber is supported by a thin stainless-steel rod (S), which is clamped at one end. Fluid drag force acting on the fiber deflects this support slightly downwards. After a calibration using a known force, the drag force is determined by measuring the displacement of a laser beam (L) reflected from a small mirror (M1) mounted on S and then from a fixed mirror (M2). The rigidity of the support and the distances between the mirrors and the ruler (R) determine the overall sensitivity of the measurement. A video camera (V) records the position of the laser beam spot on the ruler, which gives the force measurement. The soap solution is seeded with  $\text{TiO}_2$  particles, allowing the flow speed to be measured by a laser Doppler velocimeter (not shown), aimed at the midline 7 cm above the filament. (Objects and distances are not drawn to scale.) Figure reproduced from Alben, Shelley, and Zhang (Ref. 28).

constant as  $U \rightarrow \infty$ , which is the most common case for rigid bodies in experiments.<sup>25</sup>

The numerical method involves the solution of a coupled system of three equations: (i) a boundary-integral equation relating the flow speed to the fiber shape in a conformal-mapping plane, (ii) the relation of fiber arclength to a conformal-mapping parameter, and (iii) the force balance, which gives another relation between fiber shape and flow speed. This nonlinear system is solved using a quasi-Newton method, made efficient by using a pair of fast Fourier transforms to evaluate the integral equation. The details are given in Appendix A.

In Appendix B we present Helmholtz-wake solutions to the more general problem in which the fiber is held against the flow at an arbitrary point along its length, with an arbitrary orientation to the flow. We find that again the solutions tend to a universal shape, one of a two-parameter family of shapes, parameterized by the position and orientation at which the fiber is held.

This work expands upon a preliminary study of the flow-fiber problem by Alben, Shelley, and Zhang.<sup>28</sup> While we present further experimental data here, we have especially deepened our analytical understanding of this class of models, through both numerical and asymptotic analysis, and through their extensions that incorporate other physical effects.

## II. EXPERIMENT

The experimental setup is illustrated in Fig. 1. A stream of soapy water (1.5% soap concentration in deionized water)

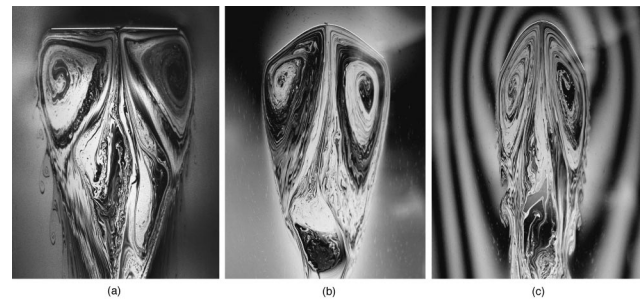


FIG. 2. Fibers in the soap film shown with interferometry. Monochromatic light from a low-pressure sodium lamp reflects from the two surfaces of the film, creating an interference pattern which shows small variations in film thickness. (a) Flow past a rigid fiber, bending rigidity  $E=2000$  erg cm. (b),(c) Flows around a flexible fiber of length  $L=4.1$  cm and rigidity  $E=2.8$  erg cm, at flow speeds of 69 cm/s (b) and 144 cm/s (c).

spreads into a vertical film between two nylon fishing lines that are parallel and under tension. The soap film flows downward under gravity to the receiving tank 2 m below the nozzle. A quasisteady planar flow is thus obtained.<sup>6,11–14</sup>

The average flow speed is regulated by the nozzle at the bottom of the upper reservoir, and the flow velocity of the film is measured using a laser Doppler velocimeter (LDV). In our case the flow is seeded with  $\text{TiO}_2$  particles (refractive index  $n=2.7$ ), which are small enough to be passively advected with the flow. The LDV measures their speed at the vertical midline of the soap film tunnel, 80 cm below the upper reservoir nozzle, where the flow speed is nearly uniform in the vertical direction. The tunnel width is 9.0 cm. Given the flow speed and tunnel width, the volume of the soapy water collected over a fixed time interval yields a direct measure of the average film thickness, which varies from 1 to 3  $\mu\text{m}$  as a function of the flow rate.

Into this background flow, at a position 7 cm below where the flow speed is measured, we insert a thin flexible glass fiber (bending rigidity  $E=2.8\text{--}2000$  erg cm, depending on fiber thickness; length  $L=1\text{--}5$  cm), which is straight in the absence of loading. The fiber is clamped at its midpoint, and held perpendicular to the background flow direction. The flow wets the bare glass fiber so that it does not cause the film to rupture, and surface tension forces hold the fiber stably within the quasi-2D plane of the soap film. A short time after insertion the flow-fiber system equilibrates, at which point the fiber exhibits a steady deflection and the flow forms a wake behind it. The fiber bends to an extent determined by its mechanical properties (length and elastic moduli) and the flow speed, and the resulting flow configuration results from the balance of mechanical stresses in the fiber with the fluid stresses on its surface. The fibers used in the experiment show no plastic deformations after the fluid loading.

The soap film is ideal for visualizing the dynamic structure of such a 2D flow. The film is illuminated by a 90-W low-pressure sodium lamp, which creates an interference pattern of monochromatic light reflected from the front and rear surfaces of the soap film. Bands of light and dark fringes show submicron variations in film thickness, and qualitatively capture the structure of the flow field. Figure 2(a) shows the flow pattern around a rigid fiber (rigidity

$E=2000$  erg cm), where even the highest attainable flow speed cannot significantly bend the fiber. Figures 2(b) and 2(c) show the flow past a more flexible fiber ( $E=2.8$  erg cm) at two different flow rates.

The wake behind the fiber is dominated by two large, slowly-rotating eddies. These are separated from the rest of the flow by free shear layers, which become more unstable as the flow speed increases. The Reynolds number of the main flow is  $O(10^4)$ , based on upstream flow speed and fiber length. The wake has a flow speed about two orders of magnitude less than that in the main flow.

The fiber is mounted at its midpoint on top of a thin supporting rod (stainless steel, 0.3 mm in diameter) that passes through the soap film near the flow stagnation point in the fiber wake, and thus has negligible effect on the flow. The supporting rod has a second role, as a linear “spring” which measures the drag on the fiber in the following manner (see Fig. 1). The rod is clamped at one end to a fixed platform, and at the other end is attached a small square mirror (10 mm side length; glass coverslip 0.06 mm thick), with its face perpendicular to the supporting rod. The drag force on the fiber deflects the support slightly downward, yielding a spring force that balances the drag. Because the displacement is small, this force is linearly proportional to the deflection of the support. The deflection is proportional in turn to the displacement of a He–Ne laser beam spot. The spot is formed when the beam is reflected from the mirror attached to the support to a second, stationary mirror, and then directed to a ruler. Lengthening the path of the beam amplifies the displacement of the laser beam spot on the ruler, which increases the resolution of the deflection measurement. Depending on the bending rigidity of the support, the distance from the fiber to the support’s clamped end, and the length of the light path, the value of the effective spring constant (ratio of load to light-spot-displacement) ranges from 0.2 to 10 dyn/mm. It is set in correspondence with the maximum drag expected for a given flow, and is calibrated using small known weights. In this way we measure the total drag force as a function of flow speed.

Figure 3(a) shows the drag data for two fibers used in the experiment. The rigid fiber is not deflected appreciably by the flow at any speed, and the drag divided by fiber length grows as  $U^2$  in accordance with classical theory. The flexible fiber has the same drag per unit length at low flow speeds, where it too is not significantly deflected by the flow. But as the flow speed increases, the drag grows much more slowly than in the rigid case because the fiber bends, presenting a different shape with a smaller profile width. We will subsequently explain this drag behavior in terms of a model based on the underlying fluid-body interaction.

In the following sections we model this flow as 2D, incompressible, and irrotational outside of the wake. Now we examine the validity of each of these assumptions. The two-dimensionality and incompressibility of soap film flows have been examined in connection with their use for experimental studies of 2D turbulence.<sup>12,29</sup> The theory finds that 2D incompressibility results when relative thickness variations are small. Time-dependent thickness variations due to the elas-

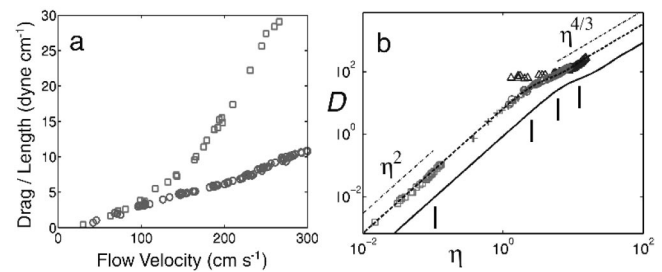


FIG. 3. Comparison of drag data from experiment and model. (a) Drag per unit fiber length versus flow velocity for a flexible fiber ( $L=3.3$  cm; circles) and a rigid fiber ( $L=2.0$  cm; squares). (b) Log–log plot of drag data in (a), nondimensionalized as  $D=C_D\eta^2$ ; also shown are data for two fibers with the same rigidity as the flexible fiber in (a) but different lengths (plus signs,  $L=1.8$  cm; triangles,  $L=5.2$  cm). The solid line is the values of  $D$  in the model, which are well-fitted by power laws  $C_1\eta^2$  for  $\eta\leq 1$  and  $C_2\eta^{4/3}$  for  $\eta\gg 1$ , as shown by dashed–dotted lines. Here  $C_1=2\pi/(\pi+4)$  and  $C_2=1.87$  (from a numerical fit). The short-dashed line is the solid line shifted by a factor of 2.8 in  $\eta$ , to correspond with the shift in the shape comparison. This shift compensates for the back pressure in the wake, as explained in Sec. IV. The vertical marks indicate, for each of the four data sets, the value of  $\eta$  at which leakage begins, corresponding to flow speed  $U=220$  cm/s. The leakage does not cause any significant deviation from the shifted drag curve. Figure adapted from Alben, Shelley, and Zhang (Ref. 28).

ticity of the soap film are small when the flow speed  $U$  is small compared to the speed of longitudinal elastic (Marangoni) waves  $v_L$ , which is  $\approx 10$  m/s for our soap films using the formulas derived by Couder *et al.*<sup>11</sup> Such time-dependent variations are thus expected to have a small effect at all but the highest flow speeds used in our experiment. However, a steady thickness profile variation may be seen in the interference fringes of Fig. 2, where the difference in thickness between neighboring light and dark fringes is  $0.11\ \mu\text{m}$ , one-quarter wavelength of sodium light (in water) and approximately 10% of the mean soap-film thickness. At the higher flow speeds, the fiber lies across multiple fringes, presumably with a monotonic thickness change starting from the midline and moving outward. The presence of the fiber also has an effect on the soap film thickness in its vicinity. Such variations are nontrivial to measure and model, so for simplicity we use only the average soap film thickness in this work. Because the fiber blocks the flow, we might expect an increased soap-molecule concentration on its upstream side. One would therefore expect a decrease in surface tension there, which would decrease the pressure drag on the fiber. However, we are unable to make local measurements of surfactant concentration near the fiber, so it would be difficult to quantify such forces. For simplicity, we also neglect the effect of variations in soap molecule concentration. We nonetheless expect that the fluid pressure forces would be predominantly set by the high-speed flow outside of this slower-moving region of increased soap concentration near the fiber. Despite these approximations, we shall see that our model provides a good rationalization of the data.

Irrotationality outside the boundary layer and wake is assumed to be a good approximation to the extent that it holds for the background flow, in the absence of the fiber. Figure 4 shows the velocity profile across the soap film tunnel, as a function of the velocity at the midline of the tunnel. We see that a background shear becomes significant for mid-

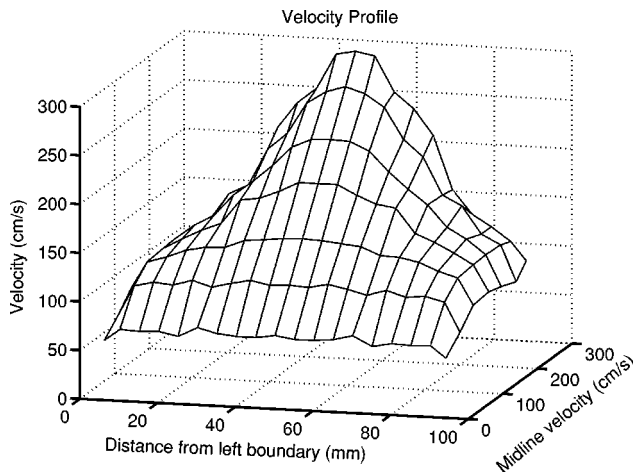


FIG. 4. The background velocity profile of the soap film, shown as a function of the velocity at the midline, and measured in the absence of the fiber. Each panel extends over 0.5 cm horizontally. Thus the longest fiber in Fig. 3(b) (5.15 cm) occupies five segments to either side of the vertical center line in its undeflected state. At the highest flow speed used in Fig. 3(b) (270 cm/s) its profile width is less than 2 cm, so it lies within two segments to either side of the center line.

line velocities  $> 200$  cm/s, but for the flexible fibers which are our primary concern, the deflected fiber occupies only  $\approx 2$  cm at the center of the soap film at these velocities. Hence irrotationality of the background flow is a reasonable approximation in the neighborhood of the fiber, except at the highest flow speeds.

It should be noted that the eigenfrequency of vibration of the support,  $\approx 3$  Hz, is far from the frequencies of vortex shedding,  $\approx 40$  Hz. If these frequencies were close to each other, the vortex shedding would be expected to cause severe vibrations. The diameter of the glass fiber ranges from 33 to 200  $\mu\text{m}$  in our experiment, which is  $\approx 20$ –100 times thicker than the soap film. Upon insertion the fiber locally blocks the flow, so that nearly all of the fluid impinging on the fiber flows around the ends rather than around the circumference, in the out-of-plane direction. But at the highest flow speeds, it is observed that the flow “leaks” at various places along the fiber in the out-of-plane direction. This may result in a smaller measurable drag compared to a fully in-plane flow, because less of the fluid momentum is transferred to the fiber. Experimentally, we face a dilemma. In order to prevent such leakage, one would like to apply a hydrophobic coating to the fiber. Unfortunately, such a coating makes the soap film very susceptible to rupture because it does not wet the fiber; fibers with a plastic coating are relatively hydrophobic compared with bare glass fibers. Fortunately, for flow speeds below 220 cm/s, leakage is rarely observed, which supports the 2D assumption of our model. We also find that as flow speeds exceed 220 cm/s, there is no noticeable deviation in the drag data of Fig. 3(b) from the data at lower flow speeds.

At the highest flow speeds we find that the force measurement becomes more scattered, which we believe has three main causes: (i) unsteady near-fiber flow due to leakage to the out-of-plane direction, (ii) unsteady vortex shedding that contributes an unsteady drag, and (iii) the increasing influence of longitudinal Marangoni waves.<sup>11</sup>

### III. MODEL

Outside the wake we take the flow to be an incompressible two-dimensional potential flow, described by the equations:

$$\frac{\partial \mathbf{u}}{\partial t} + (\mathbf{u} \cdot \nabla) \mathbf{u} = -\frac{1}{\rho} \nabla p, \quad (1)$$

$$\nabla \cdot \mathbf{u} = 0; \quad \nabla^{\perp} \mathbf{u} = 0. \quad (2)$$

Because the flow is also steady, we have Bernoulli’s equation,

$$p + \frac{1}{2} \rho |\mathbf{u}|^2 = \frac{1}{2} \rho v_s^2; \quad \mathbf{u} = \nabla \phi, \quad (3)$$

where  $\phi$  is the velocity potential, a harmonic function. Within the wake, we assume a stagnant flow, with a constant pressure. The boundary conditions for the flow outside the wake are then

$$\mathbf{u} \cdot \hat{\mathbf{n}} = 0 \quad \text{on the fiber}, \quad (4)$$

$$|\mathbf{u}| = v_s \quad \text{on the free streamlines}, \quad (5)$$

where  $\hat{\mathbf{n}}$  is the normal to the fiber, and  $v_s$  is the constant flow speed on the free streamlines. Condition (5) is a consequence of Bernoulli’s equation and the constant pressure in the wake, which is also the pressure on the free streamlines. For the Helmholtz wake model  $v_s$  equals the speed at infinity, and is larger for the extended models in Sec. VI.

Now we relate the fiber shape to the fluid pressure by the Euler–Bernoulli beam equation.<sup>30</sup> Since the fiber’s length is two orders of magnitude greater than its thickness, which is in turn two orders of magnitude greater than the soap film thickness, the fiber behaves as a beam deflected in the plane, without torsion. Locally the beam equation takes the form

$$-(T\hat{\mathbf{s}})_s + (E\kappa_s\hat{\mathbf{n}})_s = f[p]\hat{\mathbf{n}}, \quad (6)$$

where subscripts denote differentiation. Here  $f$  is the soap film thickness,  $[p]$  is the pressure jump across the fiber,  $T$  is the line tension,  $E$  the bending rigidity,  $\kappa$  the fiber curvature,  $\hat{\mathbf{n}}$  the unit normal vector, and  $\hat{\mathbf{s}}$  the unit tangent vector along the fiber. The two terms on the left represent the tensile and elastic forces on the fiber, respectively.

We assume free-end boundary conditions,

$$T = \kappa = \kappa_s = 0 \quad \text{at the fiber ends}, \quad (7)$$

which result from the vanishing of extensional force, transverse shear force, and bending moment, respectively, at the fiber ends. The fiber is also clamped perpendicular to the flow at the midpoint, so that the tangent angle is set to  $\pi/2$  there.

To simplify we decompose Eq. (6) into tangential and normal components:

$$-T_s - \frac{1}{2} E(\kappa^2)_s = 0, \quad (8)$$

$$-T\kappa + E\kappa_s = f[p]. \quad (9)$$

Integrating Eq. (8) with respect to arclength and applying the boundary condition (7) we obtain  $T = -E\kappa^2/2$ . Inserting into Eq. (9) and scaling  $\kappa$  by  $1/L$  ( $L$  is the fiber length),  $s$  by  $L$ , and pressure by  $\rho v_s^2/2$  we obtain

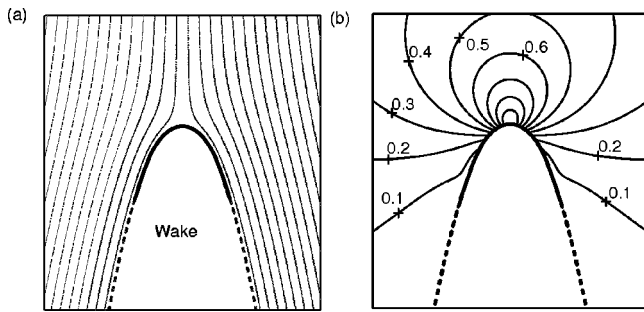


FIG. 5. The solution to the coupled flow/bending problem for  $\eta=30$ . The fiber is the solid line and the free streamlines are dashed. (a) The streamlines near the fiber. (b) Contour plot of the pressure field in the same region, with contours shown for values of 0.1 to 0.9 in increments of one-tenth. The pressure equals 1 at the stagnation point, then decreases along the filament (though not monotonically for  $\eta \gg 1$ , due to small oscillations described in Sec. V), attaining zero on the free streamlines.

$$\kappa_{ss} + \frac{1}{2} \kappa^3 = \eta^2 [p] \tag{10}$$

as the nondimensional force balance. A similar expression involving the curvature arises, for example, in studying a thin beam in a very viscous fluid.<sup>31</sup> Here  $\eta$ , defined by

$$\eta^2 = \frac{\rho f L^2 v_s^2}{2E/L}, \tag{11}$$

is the single control parameter in the problem. We have defined  $\eta$  as a nondimensional free stream speed, and we wish to know the dependence of drag on  $\eta$ . Equation (11) also shows  $\eta$  as the ratio of fluid kinetic energy to the elastic potential energy of the fiber. There is an intrinsic length scale,

$$L_0 = (2E/\rho f v_s^2)^{1/3}; \quad \eta^2 = (L/L_0)^3. \tag{12}$$

Thus varying  $\eta$  can be thought of as varying length with respect to  $L_0$ , which we term the *bending length*. Another example of an intrinsic length scale for an elastic body is the “buckling length” of a beam under compression.<sup>30</sup>

#### IV. RESULTS AND COMPARISON WITH EXPERIMENT

We first describe the main properties of the numerical solutions to the model, which are found by the method given in Appendix A. Figure 5 shows the solution for a case of moderate bending ( $\eta=30$ ). The fiber has a rounded nose at the stagnation point, with the curvature decreasing towards the asymptotically-parabolic free streamlines. The relation between fiber shape and  $\eta$  is shown in Fig. 6. As  $\eta$  increases from 0, the fiber bends, becoming progressively more aligned with the far-field flow. For  $\eta \lesssim 1$ , the fiber approximates a flat plate perpendicular to the flow at infinity; at  $\eta = 1$ , the end of the fiber has a tangent angle only one degree less than horizontal. As  $\eta$  increases past one, significant bending begins. For  $\eta=64$ , the tangent angle at the end is only 12 degrees from vertical. This fiber tangent angle increases most rapidly with respect to  $\eta$  at  $\eta=5.6$ , which gives one way of locating the transition range. For  $\eta \gg 1$ , the fiber is well-fit by a parabola near the midpoint, with a small region of high curvature there. The length of this region is

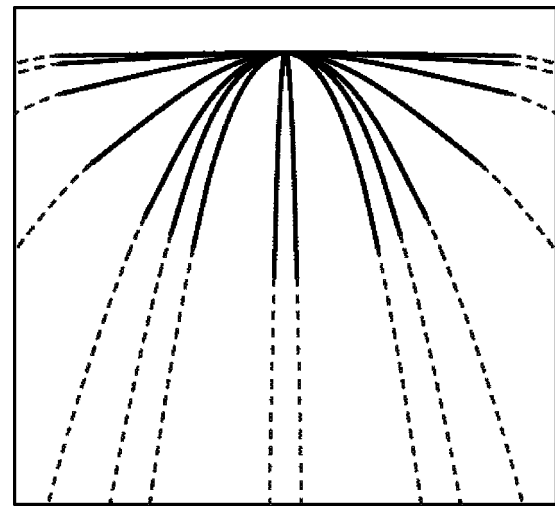


FIG. 6. Fiber shapes for a range of  $\eta$ . The solid lines are the fibers and the dashed lines are the free streamlines. The solutions shown correspond to  $\eta=1, 2, 4, 8, 16, 32, 64$ , and 30 000, increasing from flat to folded-over. A measure of the transition is  $d\theta_{\text{end}}/d\eta$ , the rate of change of the tangent angle at the fiber end with respect to  $\eta$ , which peaks at  $\eta=5.6$ .

proportional to the bending length [Eq. (12)], which also scales as the reciprocal of the midpoint curvature; outside of it the curvature decreases rapidly, and the fiber is nearly aligned with the far-field flow. In Fig. 7(d) we show a surprising property of the shapes for large  $\eta$ : a collapse onto a universal shape when the fibers are aligned at the tip and scaled by  $\eta^{-2/3}$ . We will revisit this property and analyze its consequences in Secs. VC 1–VC 4.

Now we consider the behavior of drag with respect to  $\eta$ , the dimensionless velocity. For  $\eta \lesssim 1$ , the drag follows the rigid-body  $\eta^2$ -scaling. Near  $\eta=1$ , the drag transitions sharply and apparently follows an  $\eta^{4/3}$  scaling, as shown by the solid line in Fig. 3(b). On a log–log plot, the small- $\eta$  values follow the line  $C_1 \eta^2$ , where  $C_1 = 2\pi/(\pi+4)$  is the well-known drag coefficient for a flat plate held normal to a Helmholtz free-streamline flow.<sup>17</sup> The large- $\eta$  values asymptote to the line  $C_2 \eta^{4/3}$ , where  $C_2$  is determined numerically as approximately 1.87. The drag data lie within 1% of the first fit line for  $\eta < 1.7$ , and lie within 1% of the second fit line for  $\eta > 83$ . Thus, the range  $1.7 < \eta < 83$  gives one description of the transition from  $\eta^2$  to  $\eta^{4/3}$  scaling.

We will derive these scaling properties from the asymptotics of the equations. The analysis consists of studying the form of solutions to Eq. (10) with respect to  $\eta$ . The ODE seems relatively simple, similar in form to a Duffing equation. But contained in the equation is a nonlocal singular integral operator included in the pressure jump. Despite this complication, many properties of the solutions can be derived; this is done in Sec. V.

Now we compare the Helmholtz wake model with the experiment. Though we will consider some refined models, for simplicity we restrict a detailed comparison to the Helmholtz model because it exhibits many salient features. We compare in two aspects: (i) the fiber shape as a function of velocity, and (ii) the drag force as a function of velocity. The deflected shape can be considered a measure, at each point

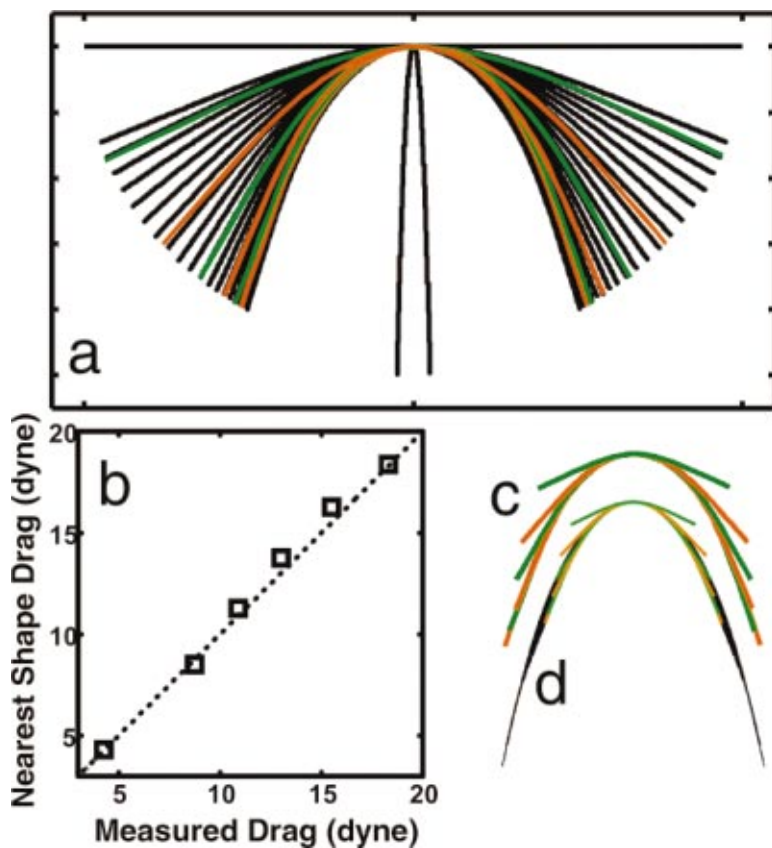


FIG. 7. (Color) Comparison of six experimental fiber shapes with model shapes. (a) Shapes from the experiment (green and orange lines) superimposed on a manifold of numerical solutions (black lines). The numerical solutions range from  $\eta=5.5$  to 33, in increments of 10%. The flat plate ( $\eta=0$ ) and a very bent solution ( $\eta=30\,000$ ) are shown for comparison. (b) Comparison of measured drag on experimental fibers in (a) with computed drag of nearest numerical solutions, determined by matching tip curvature. (c), (d) Transition to self-similarity in experimental (c) and numerical solutions (d) (not shown at the same scale). The six fibers, and their nearest numerical solutions, are dilated by  $\eta^{2/3}$  and superimposed. The black fibers are numerical solutions at higher  $\eta$ , and show the subsequent convergence to a universal shape, as predicted by the model. Figure reproduced from Alben, Shelley, and Zhang (Ref. 28).

along the fiber, of the loading by pressure forces. In Fig. 7(a), we show six shapes assumed by a single fiber as the flow speed varies by a factor of 5. The shapes are superimposed on a manifold of numerical solutions to the model, and seem to interpolate them well. More specifically, with the midpoints of the fibers aligned we find that each photographed fiber can be matched to a numerical solution that deviates from it by less than 5% in relative displacement from the midpoint. In Fig. 7(b), we compare the drag values for the six fibers shown in Fig. 7(a) with those for the nearest numerical solutions, and also obtain good agreement. This suggests that the model has correctly identified the forces that set the fiber shape as those given by the normal pressure difference and the fiber's bending rigidity. In line with this comparison, the experimental fibers also show the emergence of self-similarity; the comparison is given in Figs. 7(c) and 7(d).

In these comparisons we find that the nearest numerical shapes each have  $\eta$  greater than those for the experimental shapes, by a factor of approximately 2.8 for the six shapes we have compared. This discrepancy can be accounted for by setting the wake pressure to a value different from the pressure at infinity, as we will discuss in Sec. VI.

For the comparison of the drag-velocity relationship in the model and experiment, we display in Fig. 3(b) a set of 200 measurements of drag versus  $\eta$ , for four fibers which differ in length and rigidity. The numerical drag curve is the solid black line, and is also shown shifted to lower  $\eta$  by a factor of 2.8 (dashed line), in accordance with the shape comparison. After the shift we see good agreement between

theory and experiment, including the transition to a lower, possibly  $\eta^{4/3}$  drag scaling, though the upper limit on soap-film flow speed precludes a thorough comparison for large  $\eta$ . The vertical marks indicate, for each of the four data sets, the values of  $\eta$  corresponding to  $U=220$  cm/s, where leakage around the fiber first becomes noticeable (see Sec. II). We do not see any systematic deviation from the fitted drag curve when leakage occurs. However, the small- $\eta$  data for the longest fiber deviate from the curve. Such data correspond to the smallest flow speeds attainable in the experiment, where the soap film breaks easily and large variations are seen in measured velocity and drag. Since the fiber is fairly flat at these speeds, it occupies more than half the channel width, so the walls, thus far neglected, would be expected to have a pronounced effect. The wall effect will be discussed further in Sec. VI.

To summarize, in our comparison with the experimental data thus far, we have seen agreement in the presence of a transition to a reduced drag scaling, which has a form similar to that of the model. However, the drag is underestimated by the model. We have noted that a simple shift by a constant factor of 2.8 in  $\eta$  brings the experiment and model into alignment. This systematic deviation may be due in part to an effect which has been neglected thus far, the "back pressure" in the wake, which increases the drag. The classic example of a back-pressure induced deviation is the drag coefficient for the flat plate in the infinite-wake model,  $C_D=0.88$ , as compared with the experimental value of about two.<sup>32</sup>

An asymptotic theory of wake flows<sup>22</sup> predicts that the

wake has width  $\sim \text{Re}^{1/2}$  and length  $\sim \text{Re}$  as  $\text{Re} \rightarrow \infty$ , with a slow flow in the wake giving a back pressure  $\sim \text{Re}^{-1/2}$ . This pressure is also nearly constant, with variations through the wake of  $o(\text{Re}^{-1/2})$ . Several models have been developed to include a back pressure, whether obtained theoretically or empirically. Among the simplest, which we will adopt in Sec. VI, is that due to Riabouchinsky.<sup>27</sup>

Rigid walls constrain the fluid, forcing a faster flow around the obstacle than would be had in the unbounded case. They thereby increase the back pressure and change its limiting behavior from a  $\text{Re}^{-1/2}$  decay to an approach to a constant, nonzero value.<sup>22</sup> The wall effect is thus one of the major sources of back pressure in experiments.<sup>24</sup> The back pressure is very large for walls at a spacing of the order of the obstacle length, and is still significant for a spacing as large as 100 obstacle lengths.<sup>26</sup>

With these properties of wake flows in mind, we proceed by extending the model to incorporate walls and back pressure. This introduces two new control parameters:  $H$ , the ratio of wall-spacing to fiber length, and  $Q = (p_{\text{wake}} - p_{\infty}) / (\rho v_{\infty}^2 / 2)$ , the back pressure nondimensionalized by the dynamic pressure. The physical parameters of our experiment set  $H$ . Both  $H$  and the dynamics of the wake flow determine  $Q$ . We will not try to predict  $Q$  in our model, but rather understand how the drag and shape depend on it through numerical solutions. We will see that the drag scaling with velocity is again  $U^{4/3}$ , where  $U$  is now the velocity on the free streamline of the fiber. This will be discussed further in Sec. VI. The extended models have wakes which are smaller than the Helmholtz wake, and thus agree better in shape with those of the experiment.

We estimate the effect of skin friction by considering the limiting case of a fiber folded in two at high flow speeds. The fiber is then like a flat plate aligned with the flow, for which the corresponding skin-friction drag is  $1.33\rho U^2 L f \text{Re}^{-1/2}$ , by Blasius boundary layer theory.<sup>32</sup> This component of the drag grows as  $U^{3/2}$ , which would eventually dominate the  $U^{4/3}$  pressure drag we have identified, as long as the boundary layer is laminar ( $\text{Re} \lesssim 10^6$ ), so that the Blasius solution is valid. We use  $\text{Re} = LU/\nu$ , where  $\nu = 0.03 \text{ cm}^2/\text{s}$  is the kinematic viscosity of the soap film. For the range of parameters in our experiment, this estimate lies at least an order of magnitude below the total measured drag, and thus we neglect the effect of skin friction.

Before extending the Helmholtz model to address the points raised in the comparison with experiment, we present in Sec. V the complete equations and an asymptotic analysis of the Helmholtz model. The goal is to provide a mathematical explanation for the drag and shape scaling, which are the primary results of this work. Section VI will consider other models in light of these results.

**V. FURTHER DEVELOPMENT AND ANALYSIS OF THE MODEL**

A steady, incompressible, and irrotational flow is described by the complex potential  $w = \phi + i\psi$ , where  $\phi$  is the

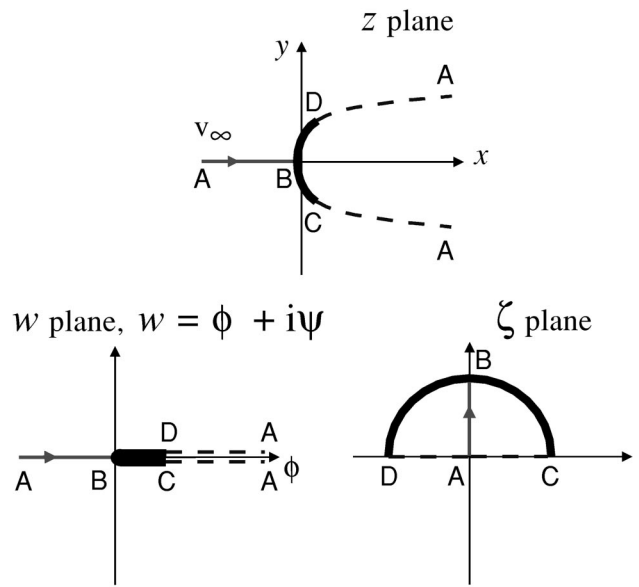


FIG. 8. The flow domain in the physical  $z$  plane, the complex-potential  $w$  plane, and the conformal-mapping  $\zeta$  plane.

velocity potential and  $\psi$  is the stream function. The analytic function  $w$  has derivative equal to the complex conjugate of the velocity:

$$\frac{dw}{dz} = \bar{v} = |v|e^{-i\Theta}, \tag{13}$$

where  $|v|$  is the flow speed and  $\Theta$  the flow direction. We now describe how to obtain the velocity field and the location of the free streamlines via conformal mapping, assuming momentarily that the fiber shape is known.

The flow is determined by the method of Levi-Civita, which uses the logarithm of the complex velocity, known as the log-hodograph variable:

$$\Omega = i \log(dw/dz) = \Theta + iT; \quad T = \log|v|, \tag{14}$$

where  $v_s$  is hereafter set to one. The method consists of solving for  $\Omega$  and  $z$  simultaneously as functions of a complex parameter  $\zeta$ , which is related by a conformal mapping.

A typical flow domain is shown in Fig. 8, along with the corresponding region in the  $w$ -plane. By setting a constant, we fix the flow's unique stagnation point at the origin in the  $w$ -plane. Since the flow region in the  $w$ -plane is the whole plane with a slit along the positive real axis, it is mapped to the upper half of the unit disk by

$$w = K/8(\zeta + 1/\zeta)^2, \tag{15}$$

where  $K$  is a positive constant determined by fixing the length of the fiber.

We obtain the map from  $z$  to  $\zeta$  in terms of  $\Omega$  by using the following identity:

$$v = e^{-i\Omega}. \tag{16}$$

Using Eq. (13) with Eqs. (15) and (16) gives

$$dz = (K/4)e^{i\Omega}(\zeta - 1/\zeta^3)d\zeta. \tag{17}$$

On the upper semicircle, where the filament lies,  $\zeta = e^{i\sigma}$  and Eq. (17) becomes

$$dz = -(K/2)e^{i\theta}e^{-\tau} \sin 2\sigma d\sigma. \tag{18}$$

Note that  $\theta$  has a jump of  $\pi$  at the stagnation point on the fiber,  $\sigma = \pi/2$ , where the flow changes direction. Thus on the fiber,

$$dz = \text{sign}(\pi/2 - \sigma) ds e^{i\theta}, \tag{19}$$

where  $ds$  is the increment in fiber length. Thus  $ds$  is related to  $d\sigma$  by

$$ds = (K/2)e^{-\tau} |\sin(2\sigma)| d\sigma. \tag{20}$$

On the interval  $[-1, 1]$  of the real axis,  $\mathcal{T}$  must vanish to satisfy the boundary condition (5). Thus we can extend the domain of definition of  $\Omega$  from the upper half of the disk to the whole disk by the Schwarz reflection principle. Condition (5) is then automatically satisfied by enforcing the symmetry of the extended  $\Omega$ , which is the main point of the Levi-Civita method. Now  $\Omega$  can be written as a power series in the disk,

$$\Omega = \sum_0^\infty a_k \zeta^k, \tag{21}$$

where the  $a_k$  are real because  $\Omega(\bar{\zeta}) = \overline{\Omega(\zeta)}$ . Evaluating at  $\zeta = e^{i\sigma}$  gives the expressions

$$\theta = \sum_{k=0}^\infty a_k \cos(k\sigma), \tag{22}$$

$$\tau = \sum_{k=1}^\infty a_k \sin(k\sigma), \tag{23}$$

which relate  $\theta$  and  $\tau$ . It is useful to decompose  $\Omega$  as  $\Omega_0 + \tilde{\Omega}$ , where

$$\Omega_0 = \theta_0 + i\tau_0 = \pi + i \ln \frac{e^{i\sigma} - i}{e^{i\sigma} + i}, \tag{24}$$

$$\theta_0 = \text{sign}(\sigma - \pi/2) \pi/2, \tag{25}$$

$$\tau_0 = \ln \left| \frac{\sin((\sigma - \pi/2)/2)}{\sin((\sigma + \pi/2)/2)} \right| \tag{26}$$

is the flat plate solution, containing the singularity at the stagnation point,  $\sigma = \pi/2$ . We integrate the desingularized form of Eq. (20),

$$s(\sigma) = K \int_{\pi/2}^\sigma (\sin \sigma' + \sin^2 \sigma') e^{-\tilde{\tau}(\sigma')} d\sigma' \quad \sigma \in [0, \pi], \tag{27}$$

where the lower limit of integration has been chosen to set  $s = 0$  at the midpoint. We determine  $K$  by setting the length of the fiber to 1:

$$1/K = 2 \int_{\pi/2}^\pi (\sin \sigma' + \sin^2 \sigma') e^{-\tilde{\tau}(\sigma')} d\sigma'. \tag{28}$$

Now we close the system by relating the fiber shape, given by  $\kappa = d\theta/ds$ , to the pressure difference in terms of  $\tau$ . Bernoulli's equation (3) gives

$$[p] = e^{2\tau} - 1, \tag{29}$$

where  $[p]$  is nondimensionalized by  $\rho v_s^2/2$ . Then the force balance (10) becomes

$$\kappa_{ss} + \kappa^3/2 = \eta^2 (e^{2\tau} - 1). \tag{30}$$

Now we express Eq. (30) in terms of  $\sigma$ . By introducing  $\nu = d\kappa/d\sigma$  the ODE (30) becomes the first-order system:

$$\begin{pmatrix} \kappa \\ \nu \end{pmatrix}' = \begin{pmatrix} \nu \\ (\eta^2 (e^{2\tau} - 1) - \kappa^3/2)(s'^2 - \nu s''/s') \end{pmatrix}, \tag{31}$$

where the primes denote differentiation with respect to  $\sigma$ . The boundary conditions (7) become  $\kappa = \nu = \nu' = 0$  at the fiber ends  $\sigma = 0, \pi$ . (To enforce  $\kappa_s = 0$  we require that  $\nu$  and  $\nu' = 0$  because  $s' = 0$  at the ends.) We integrate Eq. (31) from each end to the support at  $\sigma = \pi/2$ . After solving for  $\kappa$ , we integrate

$$\kappa = d\theta/ds = (d\theta/d\sigma)/(ds/d\sigma) \tag{32}$$

from the support to each end of the fiber, to obtain  $\theta$ . The ‘‘clamp’’ boundary condition at the support is

$$\theta|_{\sigma=\pi/2^\pm} = \pm \pi/2 \tag{33}$$

for the flow angle. We have thus used the force balance to get a second relation between  $\theta$  and  $\tau$ , in Eqs. (31)–(33).

### A. Summary of equations

To organize the procedure, we rewrite the above as a system of equations:

$$\tau = \mathcal{F}_1(\theta) \quad \text{from (22)–(23)}, \tag{34}$$

$$s = \mathcal{F}_2(\tau) \quad \text{from (27)}, \tag{35}$$

$$\theta = \mathcal{F}_3(\tau, s) \quad \text{from (31)–(33)}. \tag{36}$$

In the case of the sail considered by previous authors,<sup>33,34</sup> the force balance equation is  $[p] = -T\kappa$ , where  $T$  is the constant tension in the sail. Replacing  $\mathcal{F}_3$  by the analogous equation, one can combine the four equations into a single integral equation for  $\tau$ . In our case, the elastic force balance involves higher-order derivatives, so that the analogous integrodifferential equation is more complicated to write down. We solve (34)–(36) as a coupled system in our numerical method, a quasi-Newton iteration described in Appendix A.

### B. The asymptotic regime $\eta \ll 1$

Considering  $\eta$  as a ratio of energies, in this regime the elastic potential energy dominates the fluid kinetic energy. The problem admits a regular asymptotic expansion about the  $\eta = 0$  (flat plate) solution. Because the right side of the force-balance equation (30) is  $O(\eta^2)$  over the plate,  $\eta^2$  is the natural small parameter in which to expand  $\theta$  and its harmonic conjugate  $\tau$ . We have

$$\theta(\sigma) = \theta_{0(\sigma)} + \sum_{m=1}^\infty \theta_m(\sigma) \eta^{2m}, \tag{37}$$

$$\tau(\sigma) = \tau_{0(\sigma)} + \sum_{m=1}^\infty \tau_m(\sigma) \eta^{2m}, \tag{38}$$

where the first terms are the flat-plate solutions. Using the force balance, we obtain

$$\theta_{1,ss}(\sigma) = e^{2\tau_0} - 1 \tag{39}$$

which may be integrated thrice to give an expression for  $\theta_1$  in terms of trigonometric functions and polynomials. The succeeding terms may be integrated similarly. We have estimated the first terms in the expansion for the flat-plate drag coefficient directly from the numerical solutions to the full nonlinear problem, rather than from the expansion above. We obtain

$$C_D = C_{D0} + 2.85346 \times 10^{-3} \eta^2 + 8.14 \times 10^{-5} \eta^4 + 1.4 \pm 0.2 \times 10^{-6} \eta^6 + O(\eta^8), \tag{40}$$

$$C_{D0} = 2\pi / (\pi + 4) = 0.879802. \tag{41}$$

The precision to which we have determined the second and higher coefficients is limited by our use of double-precision arithmetic. The small magnitude of the coefficients comes from the free-end boundary conditions, which cause the first corrections to the curvature and its arc-length derivative to be small in response to the flat-plate pressure distribution.

**C. The asymptotic regime  $\eta \gg 1$**

For large  $\eta$ , the flow tends to a singular limit: uniform flow past a fiber folded in two, except for the stagnation point at the tip of the folded fiber. The discontinuity in velocity there indicates that a local stagnation-point expansion is expected for large  $\eta$ . We define the restriction of this 2D neighborhood to the fiber as “the tip region.” Using an ansatz of self-similarity suggested by the equations and confirmed by the numerics, we shall derive some of the notable asymptotic properties of the solutions:

- (1) The solutions are self-similar on a length which scales as  $\eta^{-2/3}$  (Sec. V C 1).
- (2) The leading-order fiber shape is quasiparabolic and the free streamlines asymptote to the same parabola (Sec. V C 2).
- (3) The magnitude of the second-order term scales as  $\eta^{-1}$ , and it has an oscillatory form with a characteristic wave number of  $2^{1/3} \eta^{2/3} / \pi$  away from the fiber ends (Sec. V C 3).
- (4) The tip region contributes the dominant  $O(\eta^{4/3})$  drag, while the drag on the remainder of the fiber is subdominant (Sec. V C 4).

In what follows we shall describe the solutions in terms of the shape variables,  $\theta, \kappa, \kappa_s, \kappa_{ss}$ ; the log-velocity  $\tau$ ; and the conformal-mapping parametrization  $s(\sigma)$ .

**1. The length scale of similarity**

The pressure jump at the stagnation point is  $\eta^2$ . Thus for large  $\eta$  we can expect a large curvature at the tip from the force balance. The inverse of this curvature sets the length-scale of the tip region. We presume the inner length to scale with a power of  $\eta$ , which can be determined from the force balance. The flow variables may be taken as  $u = U(\mathbf{x}\eta^\alpha)$ ,  $p = P(\mathbf{x}\eta^\alpha)$  as a tip-region ansatz. The corresponding form

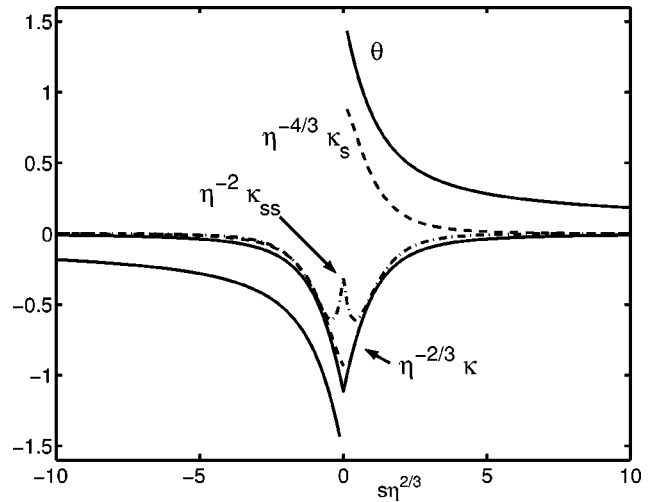


FIG. 9. The asymptotic form of the rescaled numerical solutions near the tip as  $\eta \rightarrow \infty$ , in terms of  $\theta$  (solid lines),  $\eta^{-2/3}\kappa$  (solid line),  $\eta^{-4/3}\kappa_s$  (dashed line), and  $\eta^{-2}\kappa_{ss}$  (dashed-dotted line). The first and third functions are antisymmetric and the second and fourth are symmetric about  $s\eta^{2/3} = 0$ .

for the curvature, which scales as inverse length, is  $\kappa = \eta^\alpha K(s\eta^\alpha)$ . Here  $U, P$ , and  $K$  are order-one functions. Inserting these expressions into the force balance (30), we find in the limit  $\eta \rightarrow \infty$ , the terms on the left and right may balance only when  $\alpha = 2/3$ . Thus the tip-region length scales as  $\eta^{-2/3}$ , which is also the scaling of the bending length with respect to fiber length.

The numerical solutions give clear evidence of the inner  $\eta^{-2/3}$  scale. In Fig. 9, we show the quantities  $\theta, \eta^{-2/3}\kappa, \eta^{-4/3}\kappa_s$ , and  $\eta^{-2}\kappa_{ss}$  for  $\eta$  ranging over several orders of magnitude in the range  $\eta > 100$ . We see that the functions overlap, having apparently converged to universal functions of  $S \equiv s\eta^{2/3}$  as  $\eta \rightarrow \infty$ . Then  $\tau$  also has the universal behavior, by the force balance.

Recasting the force balance in terms of  $S$ , we have

$$\theta''' + \frac{1}{2} \theta'^3 = e^{2\tau} - 1, \tag{42}$$

where primes denotes differentiation with respect to  $S$ . The associated boundary conditions are

$$\theta'' = \theta' = 0 \quad \text{at} \quad S = \pm \eta^{2/3}/2, \tag{43}$$

$$\theta = \pm \pi/2 \quad \text{at} \quad S = 0^\pm. \tag{44}$$

Now  $\eta$  has been scaled out of the equation and into the boundary conditions. One can take the limit  $\eta \rightarrow \infty$  of Eqs. (42)–(44), which takes the boundary conditions to  $\infty$  for an infinite fiber. The universal shape and flow obtained in the numerical solution appear to satisfy this limiting equation and boundary conditions, so we take the universal solution as the leading-order term in an asymptotic expansion in  $\eta$ . In the next section we pursue the asymptotic development of the solutions.

**2. Form of solutions**

As an ansatz we assume an asymptotic development consisting of the universal shape and flow (the limit of the solutions as  $\eta \rightarrow \infty$ ) plus a power series in  $\eta^{-\beta}$ ,  $\beta > 0$ :

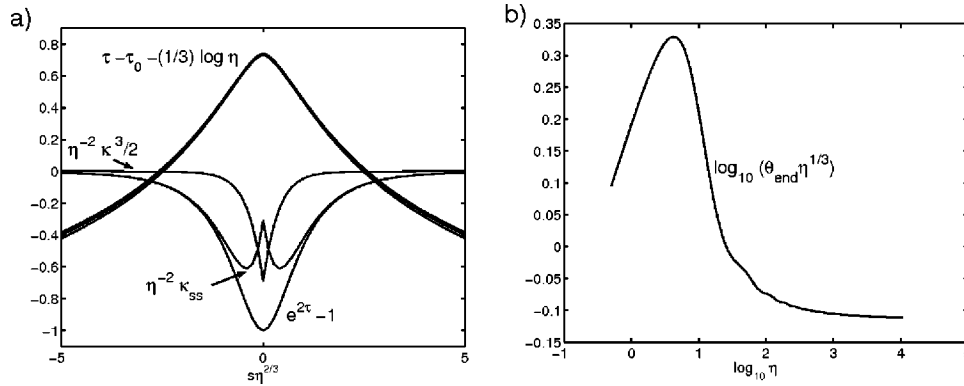


FIG. 10. Tip and end region behavior of numerical solutions. (a) Convergence of  $\tau - \tau_0 - (1/3)\log \eta$  to a constant  $C$  at the tip. Also shown is the convergence of the normalized pressure loading  $e^{2\tau} - 1 = \eta^{-2}[p]$ , and the two elastic terms  $\eta^{-2}\kappa_{ss}$  and  $\eta^{-2}\kappa^{3/2}$  which sum to it in the force balance. Note that the cubic elastic term decays more rapidly than the  $\eta^{-2}\kappa_{ss}$  term, which holds outside of the tip region as well. (b) Numerical evidence for the convergence of the tangent angle at the end of the fiber, normalized by  $\eta^{1/3}$ , to a constant  $C_0$  as  $\eta \rightarrow \infty$ . This implies that the universal fiber shape is quasiparabolic. The peak of the curve occurs near the transition to bending.

$$\theta(\sigma) = \theta_0(\sigma) + \tilde{\theta}(\sigma) = \theta_1(S(\sigma)) + \eta^{-\beta}\theta_2(S(\sigma)) + \eta^{-2\beta}\theta_3(S(\sigma)) + \dots, \quad (45)$$

$$\tau(\sigma) = \tau_0(\sigma) + \tilde{\tau}(\sigma) = \tau_1(S(\sigma)) + \eta^{-\beta}\tau_2(S(\sigma)) + \eta^{-2\beta}\tau_3(S(\sigma)) + \dots. \quad (46)$$

The successive powers of  $\eta^{-\beta}$  allow a matching of terms at each order by inserting the expansion into the force balance. The explicit dependence of the second and higher-order terms on  $\eta$  results from the  $\eta$ -dependence of the boundary conditions (43), as described in Sec. V C 3. Since  $\theta$  and  $\tau$  are linearly related by the Hilbert transform,<sup>37</sup> they are developed in the same powers. We assume corresponding expansions in the flow field for  $\Theta(Z)$  and  $\mathcal{T}(Z)$ , in the rescaled physical plane coordinate  $Z = z\eta^{2/3}$ . Now we will determine the exponent  $\beta$  and some properties of the first two terms,  $\tau_i(S)$  and  $\theta_i(S)$ ,  $i = 1, 2$ , which give the dominant contributions to the shape and drag of the fiber. To accomplish this we use the three equations that constitute the system in Sec. V A: (i) the force balance (42)–(44); (ii) the conjugacy relation (22)–(23); (iii) the conformal-mapping relation (20), in terms of  $S$ :

$$S' = (K/2)\eta^{2/3}e^{-\tau}|\sin(2\sigma)| = K\eta^{2/3}e^{-\tilde{\tau}}(\sin\sigma + \sin^2\sigma). \quad (47)$$

The first step is to determine the length-scale of the tip region in terms of  $\sigma$ . We use Eq. (47), where the value of  $e^{-\tilde{\tau}}$  at the tip is to be determined. Since  $\tilde{\tau}$  is finite at the tip,  $e^{-\tilde{\tau}} = c(\eta)$  there, where  $c(\eta)$  is nonzero and finite. Since  $e^{-\tilde{\tau}}$  is continuous it has a general expansion  $c(\eta) + o(1)$  as  $\sigma \rightarrow \pi/2$ . Insert this form into the expression for  $S'$ , integrate and then invert to obtain the first term of the Taylor series for  $\sigma - \pi/2$  in terms of  $S$  and  $c(\eta)$  about the tip:

$$\sigma - \pi/2 = S/(2K\eta^{2/3}c(\eta)) + o(S). \quad (48)$$

Now expand the right-hand side of Eq. (42) about  $\sigma = \pi/2$ , using the form for  $e^{-\tilde{\tau}}$ :

$$e^{2(\tau_0 + \tilde{\tau})} - 1 = -1 + (1/4)c(\eta)^{-2}(\sigma - \pi/2)^2 + o(|\sigma - \pi/2|^2). \quad (49)$$

$$= -1 + S^2/(16K^2\eta^{4/3}c(\eta)^4) + o(|S|^2) \quad \text{using Eq. (48)}. \quad (50)$$

By the ansatz (46) this function is independent of  $\eta$  at leading order, so if the coefficient of  $S^2$  does not vanish at leading order, we have  $c(\eta) = C\eta^{-1/3}$ , where  $C$  is independent of  $\eta$ . This implies the expansions

$$\tilde{\tau}(\sigma) = (1/3)\log \eta + C_1 + o(|\sigma - \pi/2|^0), \quad (51)$$

$$e^{2\tau} - 1 = -1 + C_2S^2 + o(S^2). \quad (52)$$

These expansions are consistent with the numerical solutions, as shown in Fig. 10. Finally, by inserting expansion (51) into Eq. (47), we conclude that if  $S = O(1)$  then  $|\sigma - \pi/2| = O(\eta^{-1/3})$ . This is the size of the tip region in  $\sigma$ . We will use this fact repeatedly in this section. The first use is to determine the behavior of the universal shape away from the tip.

We start with the relation for  $\Theta_1(\zeta)$  in terms of  $\tau_1(\sigma)$ , given by the Poisson formula,<sup>35</sup> which we evaluate at a point on the free streamlines; i.e., on the interval  $[-1, 1]$  in  $\zeta = \xi + i\nu$ :

$$\Theta_1(\xi) = -\frac{1}{2\pi} \text{Im} \int_0^{2\pi} \frac{e^{i\sigma'} + \xi}{e^{i\sigma'} - \xi} \tau_1(\sigma') d\sigma' + C_3. \quad (53)$$

Since  $\Theta_1(0) = 0$ ,  $C_3$  vanishes. Using  $\tau_1(-\sigma) = -\tau_1(\sigma)$  and  $\tau_1(\pi - \sigma) = \tau_1(\sigma)$ , the expression becomes

$$\Theta_1(\xi) = \frac{4}{\pi} \int_0^{\pi/2} \frac{(1 + \xi^2)\xi \sin \sigma'}{(1 + \xi^2)^2 - 4\xi^2 \cos^2 \sigma'} \tau_1(\sigma') d\sigma'. \quad (54)$$

Evaluating at one end of the fiber,  $\sigma = 0$ , gives

$$\theta_1(\sigma = 0) = \Theta_1(\xi = 1) = \frac{2}{\pi} \int_0^{\pi/2} \frac{\tau_1(\sigma')}{\sin \sigma'} d\sigma' \quad (55)$$

which is well-defined because  $\tau_1$  vanishes at  $\sigma=0$ . Because the flow speed  $|v|$  deviates significantly from 1 only near the tip,  $\tau \equiv \log(|v|)$  is only large near the tip. Consequently we will assume that the contribution to the integral in Eq. (55) from the tip region, within  $O(\eta^{-1/3})$  of  $\pi/2$ , is at least of the same order as that from the rest of the fiber. By Eq. (52), near the tip  $\tau_1(S) = \log|S| + C_4 + \dots$  (higher-order terms in  $S$ ), so the integral over the tip region is

$$\frac{2C\eta^{-1/3}}{\pi K} \int_0^{O(1)} [\log(S) + C_4 + \dots] dS. \tag{56}$$

Then  $\Theta_1(\xi=1) \sim C_0 \eta^{-1/3}$ , for some constant  $C_0$  [see Fig. 10(b)] which depends on the specific  $O(1)$  form of  $\tau_1$  in the tip-region. Since  $\theta_1 \sim \pm C_0 \eta^{-1/3}$  at  $S = \pm(1/2)\eta^{2/3}$  as  $\eta \rightarrow \infty$ ,  $\theta_1(S) \sim \pm C_0 |2S|^{-1/2}$  as  $|S| \rightarrow \infty$ . Thus  $dY_1/dX_1(S) = \tan(\theta_1(S)) \sim \pm |S|^{-1/2}$  as  $|S| \rightarrow \infty$ . Integrating gives  $Y_1 \sim \pm |X_1|^{1/2}$  for large  $X_1$ , which means that the universal shape is asymptotically parabolic.

We have assumed that  $\tau_1$  is small outside of the tip region to obtain the parabolic decay of the universal shape. The numerics suggest that the asymptotic relation  $\theta_1(S) \sim |S|^{-1/2}$  may be differentiated, which implies that  $\theta_1'(S)$  decays as  $|S|^{-3/2}$  and  $\theta_1''(S)$  decays as  $|S|^{-5/2}$  for large  $|S|$ . Thus the latter is the dominant term in the force balance equation (42), and since both terms are small for large  $|S|$ , the relation  $2\tau_1(S) \sim \theta_1''(S)$  follows from it. This will be used to derive the form of the second-order terms in the next section, but for now we note that  $\tau_1(S)$  decays as  $|S|^{-7/2}$ . Because of this rapid decay, the contribution to the integral in Eq. (55) from the  $|S| = O(1)$  tip region is apparently of the same order as that over the rest of the fiber, consistent with our initial hypothesis.

The same type of argument used to show that the body is asymptotically parabolic also shows that the free streamlines are asymptotically parabolic. Expanding Eq. (54) about  $\xi = 0$ ,

$$\Theta_1(\xi) = \frac{4\xi}{\pi} \int_0^{\pi/2} \sin \sigma \tau_1(\sigma) d\sigma + O(\xi^3). \tag{57}$$

Note that

$$\frac{2}{\pi} \int_0^{\pi/2} \sin \sigma \tau_1(\sigma) d\sigma \tag{58}$$

has the same value as the integral in Eq. (55), at leading order in  $\eta$  (here the  $\eta$  dependence of the integral is seen by changing the parameter from  $\sigma$  to  $S$ ). This is because the tip-region contribution to expression (58) also transforms to expression (56). From Eq. (17),  $\xi$  is related to  $s$  on the free streamlines by

$$s = -\text{sign}(\xi) (1/2 + (K/8)(\xi - 1/\xi)^2), \quad \xi \in [-1, 0) \cup (0, 1]. \tag{59}$$

Using the asymptotic expansion of  $\tau$  and the decay of  $\tau_1$  outside of the tip region, Eq. (20) implies that  $K \rightarrow 1$  as  $\eta \rightarrow \infty$ . Thus Eq. (59) gives

$$s \sim -\text{sign}(\xi) (1/2 + (1/8)(\xi - 1/\xi)^2) \tag{60}$$

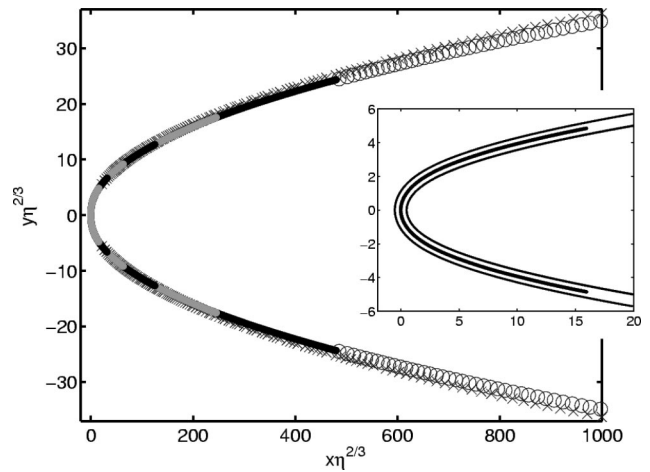


FIG. 11. Convergence of numerical fiber shapes and streamlines to a quasiseparabolic universal shape. Shown in alternating shades are the fiber shapes for  $\eta=200, 550, 1500, 4050, 11000,$  and  $30000$ , as well as the streamlines for the smallest and largest values (crosses and circles, respectively), with  $x$  and  $y$  scaled by  $\eta^{2/3}$ . The asymptotic parabola has the form  $Y=1.11X^{1/2}$ . (Inset) Numerical fiber shapes for  $\eta=200$  (thin black line),  $4050$  (white line), and  $30000$  (thick black line) in the tip region, where the universal shape fits the parabola  $Y=1.34X^{1/2}$ .

for large  $\eta$ . Hence  $\xi \sim \pm(8|s|)^{-1/2}$  near  $\xi=0^\pm$ . Thus, from Eq. (57),  $\Theta_1(\xi) \sim -2C_0\xi\eta^{-1/3} \sim \pm C_0|2S|^{-1/2}$ , giving free streamlines which are asymptotically parabolic (a general property of Helmholtz flows<sup>17</sup>), and asymptote to the same parabola as the universal shape, so that as  $\eta \rightarrow \infty$  the free streamlines merge with the universal fiber shape. This is seen in the numerical solutions of Fig. 11. We have shown this as a consequence of the far-field behavior induced by the tip region.

This result may indicate a more general principle of minimizing the sum of the kinetic energy (relative to the free stream speed) and elastic potential energy. It has been shown for finite constant-pressure wakes attached to bodies that the free streamlines minimize the added mass of the combined body and wake, within the class of piecewise-analytic wake-bounding streamlines, including those on which the flow speed is nonconstant. Thus the free streamlines also minimize the kinetic energy of the flow relative to the free stream speed.<sup>17</sup> A similar result may be obtained for the unbounded wake of the Helmholtz flow by taking the limit of the finite case, though we will not give the argument here (see Garabedian and Spencer<sup>36</sup>). Since in our case the rest of the body sits near the boundary of the wake induced by the tip, it adds little to the induced mass and kinetic energy of the free streamline flow which would be set up by the part of the body lying in the tip region alone. The rest of the body also adds little to the stored elastic energy of the fiber  $= (E/2) \int \kappa^2$ . This is partly due to the rapid decay of the leading-order curvature terms away from the tip, and also to the size of the second-order term in the curvature, which we now discuss.

### 3. Second-order equation

Our purposes in deriving the form of second-order term are twofold. First, the term further illuminates the asymptotic

properties of the solutions, as well as the role of the boundary conditions in the problem. Second, in order to give a quantitative explanation of the drag scaling it is useful to estimate the contributions from the successive terms in expansion (45)–(46).

We now derive the form of the second-order terms, beginning with the exponent  $\beta$ . None of the equations—the force balance, the Hilbert transform, or the conformal map  $s(\sigma)$ —fix this exponent, in the sense that any choice of  $\beta$  gives an expansion which can be matched at successive powers of  $\eta^{-\beta}$ . The only remaining information is the boundary conditions (43)–(44), and indeed these can be seen to set the exponent so that the sum of the first two terms in the expansion satisfies the boundary conditions. The numerical solutions show that it is possible to differentiate the asymptotic decay of the universal shape, and thus obtain  $\theta'_1(S) \sim \mp(C_0/2)|2S|^{-3/2}$  and  $\theta''_1 \sim \pm(3C_0/4)|S|^{-5/2}$  as  $S \rightarrow \pm\infty$ . Thus  $\theta'_1 \sim \mp(C_0/2)\eta^{-1}$  and  $\theta''_1 \sim \pm(3C_0/4)\eta^{-5/3}$  at  $S = \pm\eta^{2/3}/2$ . If we assume that  $\theta_2(S) = O(1)$  as  $|S| \rightarrow \infty$ , then by setting  $\beta = 1$ , the boundary condition  $\theta' = 0$  may be satisfied, while the other boundary condition is deferred to a lower-order correction.

Inserting the expansions (45)–(46) into (42), and matching at orders 1 and  $\eta^{-1}$  gives the equations

$$\theta'''_1 + \frac{1}{2}\theta_1{}^3 = e^{2\tau_1} - 1, \tag{61}$$

$$\theta'''_2 + \frac{3}{2}\theta_1{}^2\theta_2 = 2e^{2\tau_1}\tau_2. \tag{62}$$

The first-order equation is satisfied by the universal solution, with the conditions  $\theta'_1, \theta''_1 \rightarrow 0$  as  $S \rightarrow \pm\infty$ . Given the first-order solution, the second-order solution is found by solving Eq. (62) subject to the boundary conditions  $\theta'_1 + \eta^{-1}\theta'_2 = \theta''_1 + \eta^{-1}\theta''_2 = 0$  at  $S = \pm\eta^{2/3}/2$ . Thus at  $S = \pm\eta^{2/3}/2$ ,  $\theta'_2 \sim \pm C_0/2$  as  $\eta \rightarrow \infty$  and  $\theta''_2 = 0$ . Now we derive the form of  $\theta_2$  and  $\tau_2$  in Fourier space, and show that they are characterized by a single wave number over most of the fiber.

The conjugacy relation (22)–(23) can be rewritten as the Hilbert transform<sup>37</sup>

$$\tau_2(\sigma) = H^\sigma(\theta_2) \equiv \frac{1}{2\pi} \int_0^{2\pi} \cot((\sigma - \sigma')/2) \theta_2(\sigma') d\sigma', \tag{63}$$

where the integral is a principal value. Because the transform is linear, we may confine it to the second-order terms. Since  $\liminf|\theta'_2| \geq C_0/2$  at  $S = \pm(1/2)\eta^{2/3}$  as  $\eta \rightarrow \infty$ , unlike the first-order term the second-order term does not tend to zero away from the tip, and the full range of integration in Eq. (63) must be kept. From the asymptotic decay of the universal shape,  $\theta_1{}^2 = O(|S|^{-3})$ ,  $e^{2\tau_1} - 1 = O(|S|^{-7/2})$  away from the tip region. Thus for  $|S| \gg 1$  but fixed as  $\eta \rightarrow \infty$ , Eq. (62) is approximately

$$\begin{aligned} \theta_{2,SS}(S(\sigma)) &\approx 2\tau_2(S(\sigma)) \\ &= \frac{1}{\pi} \int_0^{2\pi} \cot((\sigma - \sigma')/2) \theta_2(S(\sigma')) d\sigma', \end{aligned} \tag{64}$$

with an error of  $O(|S|^{-3})$ . This is a homogeneous equation with inhomogeneous boundary conditions [given below Eq.

(62)]. It can be approximately solved if the Hilbert transform is performed in the same variable as the differentiation.

#### 4. Oscillatory form of second-order term

To approximately solve Eq. (64), we first rescale  $S$  on the fiber as  $u = \pi\eta^{-2/3}S$ , and then extend  $\theta_2$  to a  $2\pi$ -periodic function in  $u$  by the relations  $\theta_2(u + 2\pi) = \theta_2(u) = \theta_2(\pi - u)$ , which come from periodicity and evenness with respect to  $\sigma$ . We obtain

$$\begin{aligned} \theta_{2,uuu}(S(u))\pi^3\eta^{-2} &= 2H^u(\theta_2(S(u))) \\ &+ \frac{1}{\pi} \int_0^{2\pi} g(u, u') \theta_2(S(u')) du', \end{aligned} \tag{65}$$

where  $H^u$  is the Hilbert transform in  $u$  and the kernel

$$g(u, u') = \cot((\sigma(u) - \sigma(u'))/2) \frac{d\sigma}{du}(u') - \cot((u - u')/2) \tag{66}$$

is doubly continuous and unbounded only for  $u' = n\pi$ ,  $n \in \mathbb{Z}$ , which may be seen from the behavior of  $d\sigma/du$  given by Eq. (20) along with the special tip region behavior at  $\sigma = \pi/2$  given by Eq. (51). We wish to show that the integral operator  $G$  with kernel  $g$  is a smoothing operator on even,  $2\pi$ -periodic functions, and thus it is subdominant to the Hilbert transform in Eq. (65). For  $u$  fixed,  $u \neq n\pi$ ,  $n \in \mathbb{Z}$ ,  $g(u, u')$  has an inverse-square root behavior near  $u' = n\pi$ . For  $u = n\pi$ ,  $g(n\pi, u') = O((u' - n\pi)^{-1})$  near  $u' = n\pi$ . The integral in Eq. (65) is of principal-value type and thus it is well-defined in this case.

For  $u \neq n\pi$ , Eq. (27) may be used to show that  $g(u, \cdot)$  has the smoothness of  $e^{\bar{\tau}}$ , aside from the inverse-square-root singularities. Using the symmetry about the tip, one can show that for a classical solution to the force-balance equation,  $e^{\bar{\tau}}$  has at least one continuous derivative ( $e^{\bar{\tau}} \in C^1$ ). Thus  $g(u, u')$  is  $C^1$  except for the inverse-square-root singularities at  $u' = n\pi$ .

We claim that  $G(\cos mu) = O(m^{-1/2})$  as  $m \rightarrow \infty$ , for  $u \neq n\pi$ . This may be seen by writing  $g$  as a sum of singular terms plus a  $C^1$  part:  $g(u, u') = \cot(\sigma(u)/2)/(\sqrt{\pi/2Ku'}) + \cot(\sigma(u)/2)/(\sqrt{\pi/2K(u' - \pi)}) + f(u')$  for  $u' \in [0, 2\pi)$ ,  $u \neq n\pi$ . Integrating the first two terms against  $\cos mu$  gives terms of  $O(m^{-1/2})$ ; this comes from substituting  $x = \sqrt{m}u$ , which leaves a Fresnel integral. The contribution from  $f \in C^1$  is  $O(m^{-1})$ .

Using this smoothing property of  $G$ , we show that a leading-order oscillatory behavior of  $\theta_2$  is consistent with Eq. (65), with wave number scaling as the bending length,  $\eta^{2/3}$ . We assume as an ansatz

$$\theta_2 = A \cos((u - \phi)/\epsilon) + \epsilon^{1/2}b(u), \quad \epsilon = 2^{-1/3}\pi\eta^{-2/3}. \tag{67}$$

The first term satisfies  $\theta_{2,uuu} = 2H^u(\theta_2)$  exactly, with an  $O(1)$  phase  $\phi$  set by the boundary conditions, and  $b(u)$  is assumed to be  $O(1)$  at leading order. Matching at the next order,  $O(\epsilon^{1/2})$ , gives a leading-order equation for  $b$ :

$$-H^u(b) - G(b) = j(u), \tag{68}$$

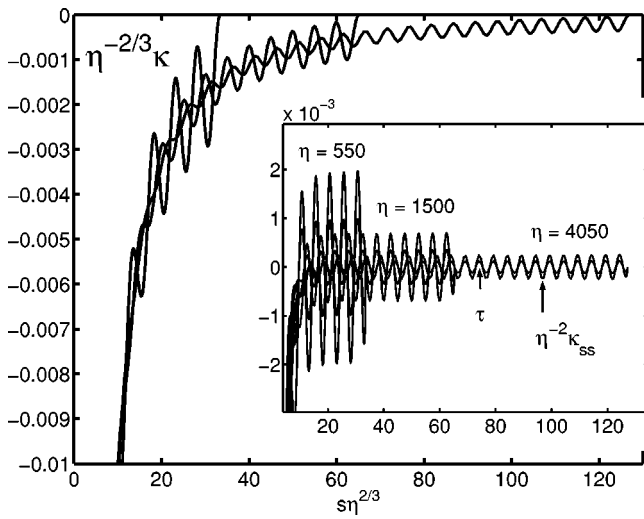


FIG. 12. The numerical solutions away from the tip region for  $\eta=550, 1500, 4050$ , in terms of the rescaled curvature  $\eta^{-2/3}\kappa$  and (inset) the dominant terms in the force balance,  $\tau$  and  $\eta^{-2}\kappa_{ss}$ . Because of the rapid decay of the first-order term, the oscillatory second-order term is clearly visible. For each of the functions shown, the amplitude of the second-order term decays as  $\eta^{-1}$ , and the wave number of the oscillations  $k_s$  appears to converge to  $2^{1/3}$ , matching it to within 1% for  $\eta=550$  and to within 0.1% for  $\eta=4050$ .

where  $j$  is  $\epsilon^{-1/2}$  times ( $G$  applied to the cosine term). By the smoothing of  $G$ ,  $j$  is then  $O(1)$  except near the fiber end points,  $u=0, \pi$ .

This oscillatory form for the second-order term is captured well by the numerics (see Fig. 12). In particular, the characteristic wave number of the numerical solutions appears to converge to that predicted by the ansatz (67) ( $2^{1/3}\eta^{2/3}/\pi$  in  $u$ , or  $2^{1/3}$  in  $S$ ) with an error of  $<0.1\%$  for  $\eta \geq 4050$ . The agreement improves for larger  $\eta$ , presumably because the next (third-) order term becomes smaller relative to the second.

We have determined the functional form of the first two terms in the asymptotic expansion of the curvature. Combining the asymptotics and the numerics, we find that the numerical solutions away from the tip region are well fit by

$$\eta^{-2/3}\kappa = 0.30|S|^{-(3/2)} + 0.62\eta^{-1}\cos(2^{1/3}\eta^{2/3}(s - \phi_1)), \tag{69}$$

for all  $S$  away from an ‘‘end region’’  $||S| - \eta^{2/3}/2| < 3$ , which corresponds to a region with length  $O(\eta^{-2/3})$  about  $u=0, \pi$ . Here  $\phi_1 = \phi/\pi$  is a constant phase.

For completeness, we describe the solutions’ behavior near the fiber end. In the end region  $\tau_2$  is characterized by a square-root behavior, which has to do with the properties of free-streamline separation from a sharp edge. The continuity of flow speed requires that  $\tau=0$  at the ends, but does not specify the form of  $\tau$  near the end. It has been shown<sup>17</sup> for a  $C^2$  barrier that unless  $\Omega' = \Omega'' = 0$  at the separation point, the curvature of a free streamline diverges there. Here it can be seen to diverge like an inverse square root. By differentiating (54) with respect to  $\xi < 1$  and letting  $\xi \rightarrow 1^-$ , we obtain  $\theta_\xi(1) = 2\theta(1) \neq 0$  due to the dominant, single-signed tip re-

gion contribution to the integral in Eq. (55). Consequently  $\tau_\sigma(\sigma=0) \neq 0$  by the Cauchy–Riemann equations, so locally  $\tau = C\sigma + \dots$ . Outside of the tip region,

$$ds = |\sin 2\sigma| d\sigma + O(\eta^{-1/3}) \tag{70}$$

which implies a leading-order square root behavior in  $\tau(S)$  at the fiber ends. By the Cauchy–Riemann equations, this is equivalent to an inverse square-root behavior for the separation curvature  $\theta_\xi(1)$ .

One interesting result of expression (69) is that the second-order terms dominate the first-order terms in the force balance away from the tip region. The dominant first-order terms are  $\theta_1'''$  and  $\tau_1$ , which, from the numerics, are  $O(\eta^{-7/3})$  at an arbitrary but fixed distance from the tip, as  $\eta \rightarrow \infty$ . Hence the  $O(\eta^{-1})$  second-order terms dominate (see Fig. 12). The third and higher-order terms in the expansion (46) may be derived in a similar fashion, but we will not pursue this here.

### 5. Drag scaling

Having described the scalings of the first two terms in the asymptotic expansion, we are now in a position to understand the  $\eta^{4/3}$  drag scaling.

We use the rescaled  $x, y$ , and  $\kappa$  as  $X = x\eta^{2/3}, Y = y\eta^{2/3}$ , and  $\mathcal{K} = \eta^{-2/3}\kappa$ , and recall that the tip region has length  $O(\eta^{-2/3})$  in  $s$  and  $O(1)$  in  $S$ . We will now show that the tip region controls the drag, in the sense that any region which is slightly larger than it gives the dominant contribution to the drag. More precisely, for any  $\epsilon > 0$ , the drag in an interval  $I$  of length  $C\eta^{-2/3+\epsilon}$  about the tip,  $s=0$ , is asymptotically dominant to that on the remainder of the fiber.

The drag on  $I$  is given by

$$\begin{aligned} \mathcal{D}(I) &= \eta^2 \int_I p dy = \int_{-C\eta^{-2/3+\epsilon/2}}^{C\eta^{-2/3+\epsilon/2}} \left( \frac{1}{2}\mathcal{K}^3 + \kappa_{ss} \right) \frac{dy}{ds} ds \tag{71} \\ &= \eta^{4/3} \int_{-C\eta^{\epsilon/2}}^{C\eta^{\epsilon/2}} \left( \frac{1}{2}\mathcal{K}^3 + \mathcal{K}'' \right) \frac{dY}{dS} dS. \tag{72} \end{aligned}$$

The drag contribution from the remainder of the fiber is given by

$$\mathcal{D}(I^c) = \eta^{4/3} \int_{[-\eta^{2/3}/2, \eta^{2/3}/2] \setminus I} \left( \frac{1}{2}\mathcal{K}^3 + \mathcal{K}'' \right) \frac{dY}{dS} dS. \tag{73}$$

We estimate the curvature terms from Eq. (69), and obtain  $\mathcal{K}^3 \leq C_1|S|^{-9/2} + C_2\eta^{-1}|S|^{-3}$  and  $\mathcal{K}'' \leq C_1|S|^{-7/2} + C_2\eta^{-1}$  for positive constants  $C_1$  and  $C_2$ . Also,  $dY/dS \sim \theta \sim |S|^{-1/2}$ . Inserting these estimates into Eq. (73) we find that  $\mathcal{D}(I^c) \leq C_3\eta^{4/3-3\epsilon}$ , for  $\epsilon$  sufficiently small, which comes from the bound for  $\mathcal{K}''$ . The integrand is  $O(1)$  in the tip region, so a similar argument shows that  $\mathcal{D}(I)$  is  $O(\eta^{4/3})$ . We have shown that the tip region gives the dominant drag contribution, even though the tip region is  $O(\eta^{-2/3})$  smaller than the remainder of the fiber.

The self-similar quasiparabolic fiber shape gives the scaling of the profile width. First, express the parabola to which the fiber asymptotes as  $X = CY^2$ . At the fiber ends  $X \sim S = \pm \eta^{2/3}/2$ , so that  $Y \sim \pm \eta^{1/3}$ , or  $y \sim \pm \eta^{-1/3}$ . Hence the

profile width decreases as  $\eta^{-1/3}$ , which would imply a drag scaling of  $\eta^{5/3}$  in the absence of streamlining. By “streamlining” we mean a reduction in drag due to a change of shape which keeps the profile width fixed. For example, a flat plate may be streamlined by changing it to a circular arc with chord length equal to the plate length. Streamlining thus gives a size-independent measure of the effect of shape on drag. For the fiber, the streamlining caused by bending decreases the drag by a factor of  $\eta^{-1/3}$ , so that the reduction of the drag exponent from 2 is due in equal parts to decrease of profile width and to streamlining.

**VI. EXTENDED MODELS**

Now we examine the effect of incorporating walls and wake pressure into our flow model, in terms of  $H$ , the ratio of wall-spacing to fiber length, and the wake pressure coefficient  $Q = (p_{\text{wake}} - p_{\infty}) / (\rho v_{\infty}^2 / 2)$ . Unlike the Helmholtz flow, these models have a free-streamline speed  $\eta_s$  which is different from the upstream flow speed,  $\eta_{\infty}$  [both speeds are nondimensionalized as in definition (11)]. The two are related by  $\eta_s = \eta_{\infty} \sqrt{1 - Q}$ .

We begin by examining a model in which  $H$  is the only free parameter: the case of “choked flow.”<sup>26</sup> Here the wake is of infinite length, but the flow is bounded by infinite parallel rigid walls. Since the wake occupies part of the channel width downstream of the body, conservation of mass requires that  $\eta_s > \eta_{\infty}$ . The resulting non-zero value of  $Q$ , which is set by the wall-spacing, thus reflects the contribution of the walls to the wake pressure. We will then consider the effect of varying  $Q$  in the unbounded Riabouchinsky flow (for which  $H = \infty$ ). The effect is to shift the drag curve from the Helmholtz curve by the factor  $\sqrt{1 - Q}$  in  $\eta_{\infty}$ , which is the same type of shift as was used to align the Helmholtz and experimental drag data in Sec. IV. Finally, we study the wall-bounded Riabouchinsky flow, with  $Q$  and  $H$  as free parameters. We find that the models give similar shapes and nearly identical values for the drag when  $Q$  is the same in all of them. For  $Q$  fixed, changing the wall spacing gives only a small perturbation to the solution, except in the special case of very closely spaced walls.

In these extended models we specialize to the symmetric case of a fiber clamped at its midpoint and held perpendicular to the flow. The effect of asymmetry is described in Appendix B for the Helmholtz model, and the effect of asymmetry in the extended models may be deduced from the results there. This allows us to model only half of the flow domain, in which case the flow angle  $\theta$  is known on a connected part of the boundary, and the conjugate  $\tau$  is known on its complement. Hence the boundary value problem for  $\Omega$  may still be solved using the Schwarz reflection principle. By contrast the asymmetric case involves a mixed Riemann–Hilbert problem, which adds some complications to the numerical method.

**A. Wall-bounded infinite wake model**

To examine the effect of increased momentum transfer to the fiber due to walls, we construct flows bounded by two infinite parallel walls placed symmetrically about the fiber,

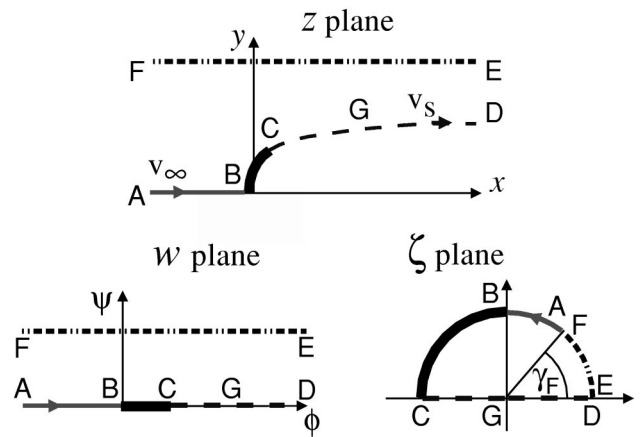


FIG. 13. The infinite wall-bounded flow domain in the  $z$ ,  $w$ , and  $\zeta$  planes.

and having an infinite wake. From our numerical results, there is apparently a unique flow of this type for each choice of wall-spacing, as is known to be the case for flows past plates and wedges.<sup>26,38</sup>

We map half of the flow field to the upper half of the unit disk, sending the fiber, stagnation streamline, and upper wall to the upper semicircle (see Fig. 13). Starting from

$$w = a \log \frac{\cos \gamma_F + (\zeta^2 - \zeta + 1)}{\cos \gamma_F - (\zeta^2 - \zeta + 1)}, \tag{74}$$

the development then parallels that of the Helmholtz case. Here  $a$  is used to set the fiber length and  $H = (\text{wall spacing}) / (\text{fiber length})$  sets the free parameter  $\gamma_F$ , the argument of the point in  $\zeta$  corresponding to upstream infinity in  $z$ . The stagnation-point singularity is explicitly removed by

$$\Omega_0 = (-i/2) \log \frac{i\zeta - 1}{i - \zeta}, \tag{75}$$

which leaves  $\bar{\Omega}$  continuous on the boundary of the unit disk.

Figure 14(a) shows an example of the wall-bounded flow for  $H = 9/5.15$ , corresponding to the longest fiber used in our experiment. The pressure field tends to different limiting values upstream and downstream, but is otherwise similar to that of the Helmholtz case. Because of the lower wake pres-

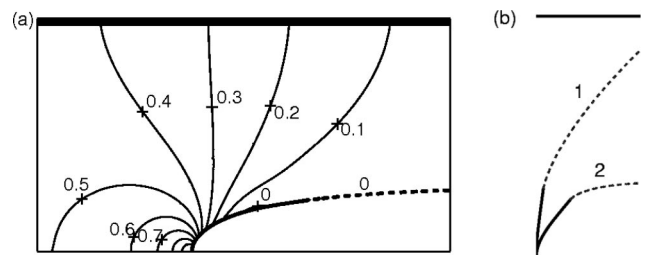


FIG. 14. (a) Contour plot of the choked-flow pressure field for  $\eta_{\infty} = 54$  and  $H = 9/5.15$ . The pressure is scaled to equal 1 at the stagnation point and 0 on the free streamlines. A small region in which the pressure is negative is contained between the leftmost 0 contour and the fiber, showing the non-monotonic behavior of the pressure due to the oscillatory second-order term. (b) A comparison of the Helmholtz (1) and choked flow (2) solutions for  $\eta_{\infty} = 3$ . The wall for (2) is shown, and  $H = 2.7$ .

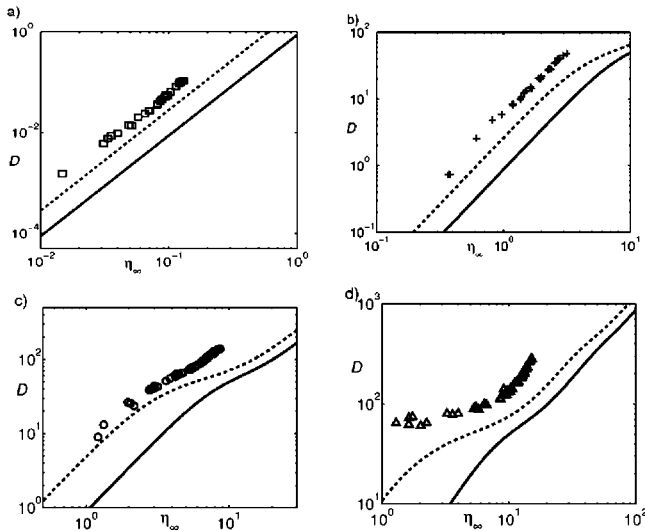


FIG. 15. The choked-flow drag curves (lines covered by small symbols) compared to the Helmholtz drag curve (solid line) and the four sets of experimental data shown in Fig. 3(b). (a)  $H=9/1.95$ , corresponding to the most rigid fiber ( $E=2000$ ) used in the experiment; (b)  $H=9/1.79$ ,  $E=2.8$ ; (c)  $H=9/3.3$ ,  $E=2.8$ ; and (d)  $H=9/5.15$ ,  $E=2.8$ .

sure, the fiber deflection is significantly increased over that in the Helmholtz case with the same upstream velocity. Figure 14(b) shows this comparison for  $\eta_\infty=3$ .

Because we have used four different fiber lengths in the experiment [see Fig. 3(b)], we compare the drag versus  $\eta_\infty$  in the choked flow model for each fiber separately. In Fig. 15 we see that the effect of the walls is to shift the drag curve significantly leftward from the Helmholtz curve. Hence the addition of walls to the Helmholtz model can provide a large increase in drag. In all cases the increase is not sufficient to close the gap with the experiment. This might be expected because the experimental wake is finite, and thus should have a still lower back pressure than the choked flow.

We note two other main results for the bending fiber in a choked flow. The first is that the choked flow drag curve converges to the Helmholtz curve as  $\eta_\infty \rightarrow \infty$ . This is because as the fiber approaches the folded limit, the streamlines near the fiber become more parallel to the walls. Hence the flow converges to that of the corresponding Helmholtz flow, as the deviation required to meet the no-penetration boundary condition at the wall becomes smaller. The second result is that the wake pressure coefficient  $Q \sim \eta_\infty^{-1/3}$  as  $\eta_\infty \rightarrow \infty$ . This may be explained using a conservation-of-mass argument. To begin, there is a range starting at the fiber end over which the free streamlines approximate the self-similar parabolic shape of Helmholtz streamlines for the same  $\eta_\infty$ . This range increases in length as  $\eta_\infty \rightarrow \infty$ , but is eventually matched to a subsequent region in which the free streamlines become asymptotically parallel to the walls. The limiting distance  $d$  between the free streamline and the wall in this region is apparently set by the distance between the free streamlines in the self-similar parabolic region. This wake width has the same  $\eta_\infty^{-1/3}$  scaling as the fiber profile width, since both are asymptotically parabolic. Thus  $H=2d \sim \eta_\infty^{-1/3}$ . Equating the

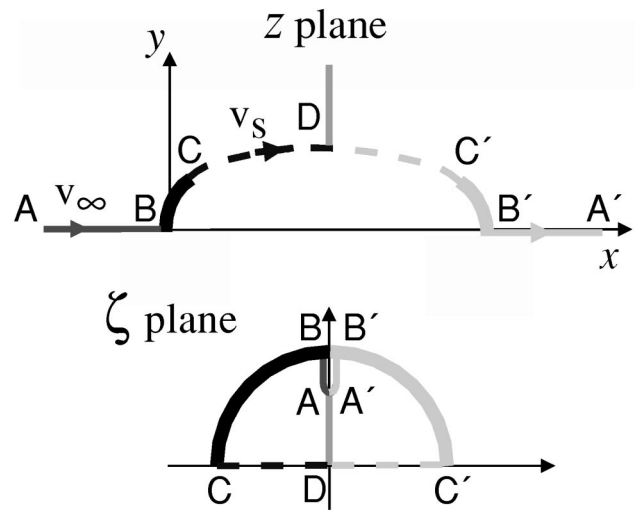


FIG. 16. The symmetric Riabouchinsky flow domain in the  $z$  and  $\zeta$  planes. The ordinate  $I_0$  of  $A$  is a free parameter set by the wake pressure  $Q$ .

mass flux through the channel far upstream and far downstream, and using  $\eta_s = \eta_\infty \sqrt{1-Q}$ , gives  $H\eta_\infty = 2d\eta_s = 2d\eta_\infty \sqrt{1-Q}$ , which with the previous scaling implies  $Q \sim \eta_\infty^{-1/3}$ . This gives the rate of decay of the back pressure due to the wall effect for the flexible fiber.

**B. Riabouchinsky mirror-image wake model**

In order to freely vary the wake pressure, we must choose a different flow geometry. For the infinite wake  $Q=0$ , but for a finite wake  $Q<0$  and the free-stream speed is higher than the upstream flow speed. Several simple finite-wake models have been developed, having many properties in common. Each model takes  $Q$  as a free parameter and each yields realistic pressure distributions when  $Q$  is set to conform with a particular experiment.<sup>25</sup> Also, the flow in each case tends asymptotically to that of the Helmholtz wake solution as  $Q \rightarrow 0$ . The simplest and best-known of these models is the mirror-image model of Riabouchinsky,<sup>27</sup> which we adopt.

The conformal mapping planes are shown in Fig. 16. The system of equations is derived starting from

$$w = a(((\zeta + 1/\zeta)/(I_0 - 1/I_0))^2 + 1)^{-1/2}, \tag{76}$$

where  $iI_0$  is the location of the point at infinity in the  $\zeta$ -plane, and is set by the choice of  $Q$ .

Figure 17 shows the drag versus  $\eta_\infty$  for three choices of  $Q$ , and the same data plotted versus  $\eta_s$ , in which case the curves are nearly identical. This is because for fixed  $\eta_s$  and different  $Q$ , the flow near the fiber is nearly independent of the differing values of  $\eta_\infty$  far upstream. Thus, for fixed  $\eta_s$ , the pressure jump distribution is nearly identical. As Fig. 17 shows, the effect of varying  $Q$  for fixed  $\eta_\infty$  is simply to shift the Helmholtz drag curve by a factor of  $\sqrt{1-Q}$  in  $\eta_\infty$ . We find that the value  $Q = -6.8$  corresponds to the  $\eta$ -shift of 2.8 between the Helmholtz drag curve and the experimental data shown in Fig. 3(b). For wakes in standard flow tunnels, the range  $-2 < Q < 0$  is typical,<sup>25</sup> our value of  $-6.8$  is probably caused by soap film effects such as surface tension.

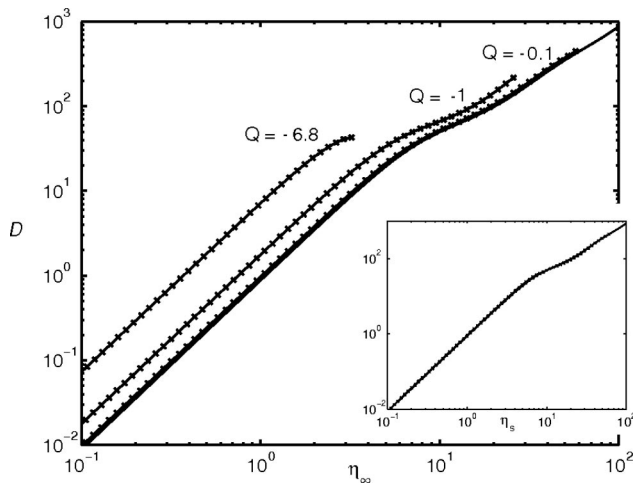


FIG. 17. Drag vs  $\eta_\infty$  for Riabouchinsky solutions with  $Q = -6.84, -1, -0.1,$  and  $0$  (Helmholtz) moving from left to right. For each  $Q$  the data are shown for the maximum intervals in which the solutions exist. (Inset) Drag vs  $\eta_s$  for the same solutions.

An inconvenience with this particular choice of model is that for each value of  $Q$ , the mirror image flow solutions do not exist above a critical value of  $\eta_\infty$ . As this value is approached from the below, the mirror-image fibers approach one another and touch at the critical value (see Fig. 18). This is an artifact of the mirror-image model; other wake models, such as the several listed by Wu,<sup>25</sup> presumably would not share this difficulty. However, the characteristics of the mirror-image solutions relative to those of the Helmholtz flow are clear enough from the range in which solutions exist. In particular, Fig. 17 shows that the effect of a constant back pressure is to shift the drag data, leaving the  $\eta^{4/3}$  scaling intact. The scaling also holds asymptotically for a non-constant back pressure which tends to a constant as  $\eta \rightarrow \infty$ .

**C. Wall-bounded mirror-image wake model**

Finally, we compute symmetric wall-bounded flows with a mirror-image wake while allowing a nonzero wake pressure (see Fig. 19). The corresponding map is

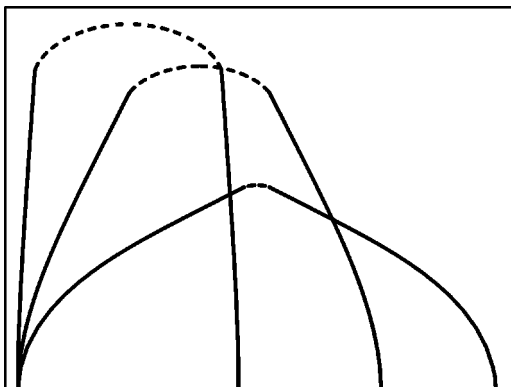


FIG. 18. Riabouchinsky solutions for  $Q = -6.8$  and  $\eta_\infty = 0.65, 1.77,$  and  $3.56$ , increasing from flat to bent. Solution fiber collides with the mirror-image fiber at  $\eta_\infty = 3.6$ .

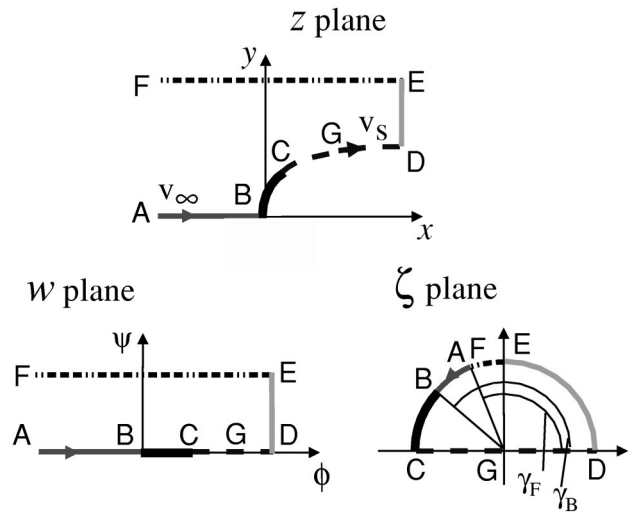


FIG. 19. The wall-bounded mirror-image flow domain in the  $z, w,$  and  $\zeta$  planes.

$$w = a \log \frac{1 - A(\zeta)}{1 + A(\zeta)}; \tag{77}$$

$$A(\zeta) = (\zeta - 1) / \sqrt{(1 - \sec \gamma_F)(\zeta^2 + 1)},$$

where the fiber length fixes  $a$ . The two free parameters  $\gamma_B$  (location of the midpoint of the fiber) and  $\gamma_F$  (upstream infinity) are set by  $Q$  and the wall-spacing  $H$ . The stagnation point singularity is now subtracted off by

$$\Omega_0 = (-i/2) \log \frac{e^{i\gamma_B \zeta} - 1}{e^{i\gamma_B} - \zeta}. \tag{78}$$

In Fig. 20 we compare a solution from this combined model with one from each of the previous two flow models: a choked-flow solution with the same values of  $\eta_\infty, H,$  and  $Q$ , and an unbounded Riabouchinsky solution with the same values of  $\eta_\infty$  and  $Q$ . The fiber deflections are nearly the same in all three solutions and the drag values agree to within 0.1%. This suggests that the flow near the fiber is essentially determined by  $\eta_\infty$  and  $Q$ . When these parameters are set, the presence or absence of walls and/or a finite wake does not seem to change the near-body flow significantly.

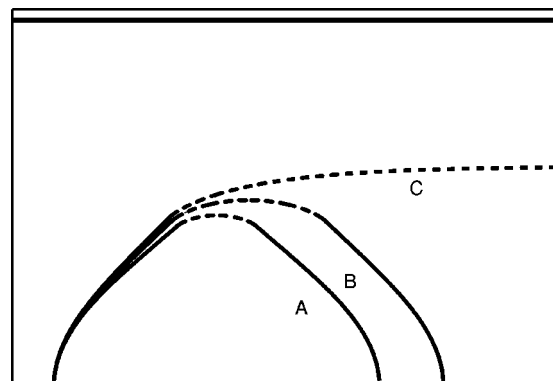


FIG. 20. A comparison of the unbounded Riabouchinsky flow (A), wall-bounded Riabouchinsky flow (B), and choked flow (C). For (B) and (C),  $H = 9/5.15$ . For all three flows  $\eta_\infty = 3.4$  and  $Q = -4.8$ .

These models have shown that the fiber deflection and drag are changed by wake pressure to become very close to the Helmholtz solution with speed given by  $\eta_s$  instead of  $\eta_\infty$ . For the typical cases of a wake pressure coefficient  $Q$  which is nearly constant, or tends to a constant or zero as flow speed is increased, an  $\eta_\infty^{4/3}$  drag scaling is expected. Otherwise the dependence  $Q(\eta_\infty)$  can be used to determine  $\eta_s$ , at which value the drag given by the Helmholtz curve is approximately obtained.

## VII. CONCLUSION

In this work we have studied the streamlining of a flexible fiber in a 2D flow. Modelling it as a thin beam in a free-streamline flow, we have identified a single nondimensional control parameter  $\eta$  which governs the underlying mechanical interaction. In both theory and experiment we find a sharp transition to bending when  $\eta$  exceeds  $O(1)$ , corresponding to a transition to dominance of pressure forces over elastic bending forces. An important consequence is a reduction from rigid-body  $U^2$  drag scaling to a  $U^{4/3}$  behavior. Using the force balance equation we identified a similarity length-scale  $\sim \eta^{-2/3}$ . By constructing an asymptotic expansion in the rescaled fiber length, we found that the leading-order fiber and wake shapes asymptote to the same parabola when distances are scaled by  $\eta^{2/3}$ . Thus the fiber tends to the boundary of the wake induced by the shrinking “tip region” as  $\eta \rightarrow \infty$ . The first correction to this term has an oscillatory character and decays as  $\eta^{-1}$  in magnitude. Using the form of the first two terms in the expansion we showed that the tip region gives the dominant  $O(\eta^{4/3})$  contribution to the drag. One consequence of the leading-order fiber shape is that the profile width scales as  $\eta^{-1/3}$ . This shows that the drag reduction is due in equal parts to a smaller profile width and to a more streamlined shape.

The main discrepancy between the simplest (Helmholtz wake) model and experiment is that in the experiment, the transition to self-similar behavior occurs at a smaller value of the control parameter. Motivated by previous wake-flow studies, we incorporate a constant nonzero wake pressure, and show that this causes a uniform shift of the drag data, as seen in the experiment. The contribution of the walls to the wake pressure is shown to be significant as the fiber bends, but does not account for the entire mismatch between theory and experiment. The missing part of the wake pressure is presumably provided by surface tension effects in the soap film as well as the process of shedding vorticity into the wake. In future work we shall consider the details of how this occurs for a flexible body in a high-Reynolds-number flow.

We have not addressed mathematical questions of existence and uniqueness for the system of free-streamline/beam equations. It is useful nonetheless to place the mathematical problem in the context of more general theoretical work and to this end we note that our problem can be formulated concisely in two ways. The first, which we have used in this work, consists of substituting for  $\tau$  in the force balance with the Hilbert transform of  $\theta$ , and then changing variables from  $s$  to  $\sigma$ . The problem may then be reduced to one singular

integro-differential equation on  $[0, \pi]$  with the free-end boundary conditions, which we have not written out in this work because it is rather complicated. The second formulation is that of solving Laplace’s equation for  $\Omega$  in the unit disk with the nonlinear force balance as the boundary condition relating the real and imaginary parts  $\theta$  and  $\tau$ . This is a type of nonlinear Riemann–Hilbert problem, and theoretical results have been obtained for other boundary-value problems from fluids and elasticity using this type of formulation (see Wegert<sup>39</sup>).

## ACKNOWLEDGMENTS

We thank Stephen Childress, Albert Libchaber, Peter Palfy-Muhoray, David Muraki, and Petri Fast for helpful conversations, and also thank Yu-Qi (Matthew) Xia who assisted in a preliminary experimental study of the fiber/flow system. We acknowledge support from the Department of Energy Grant No. DE-FG02-88ER25053 and from the National Science Foundation.

## APPENDIX A: COMPUTATIONAL METHODS

Aside from certain cases of straight or circular bodies, a free-streamline flow cannot be solved analytically in closed form. Several computational methods exist for determining the flow past a fixed body, or for solving the inverse problem.<sup>19,40</sup> Ours is based on that of Hureau *et al.*,<sup>41</sup> which has a convenient formulation in terms of the tangent angle of the body contour as a function of arclength.

Equations (34)–(36) form the basis of an iterative scheme. Given an initial guess for  $\tilde{\theta}(\sigma)$ , we compute  $\tilde{\tau}$  and  $s$ , and use the updated values to recompute  $\tilde{\theta}$ . All functions are represented on the same equidistant mesh on  $[0, \pi]$ . Thus we solve a nonlinear system of equations

$$F(\tilde{\theta}) = \tilde{\theta} - \mathcal{F}(\tilde{\theta}) = 0. \quad (\text{A1})$$

Here  $\mathcal{F}$  symbolizes the computation of  $\tilde{\theta}$  using updated  $s$  and  $\tilde{\tau}$ . We iterate until  $F(\tilde{\theta}) < \epsilon$ , with  $\epsilon = 10^{-12}$  for the results given in this paper. At each step Eq. (A1) is solved using a quasi-Newton method, the damped Broyden method,<sup>42</sup> which shows superlinear convergence so long as the Jacobian matrix at the solution is nonsingular.

The initial guess is crucial for obtaining convergence, particularly for large  $\eta$ . Since we are interested in the behavior over a large range of  $\eta$ , we begin by solving for  $\eta \ll 1$  (for which convergence is rapid, starting from the flat plate shape), and then take small steps to larger  $\eta$ , extrapolating from the previous solutions to form an accurate initial guess. The Jacobian matrix is initialized using divided differences of  $F$  evaluations, and the inverse is computed explicitly once at the start of the Broyden iteration. Updating the Jacobian requires only matrix-vector multiplications.

Each computation of  $F$  involves three separate computations, one each for  $\tilde{\tau}$ ,  $s$ , and  $\tilde{\theta}$ . The first uses two FFTs and involves  $O(n \log n)$  work; the last two involve  $O(n)$  operations. Thus the total work for  $F$  is  $O(n \log n)$ . The overall time is dominated by the  $n$  evaluations of  $\mathcal{F}$  needed to initialize the Jacobian matrix in the Broyden method. The iteration typically converges in 10–20 iterations. For  $n = 1024$ ,

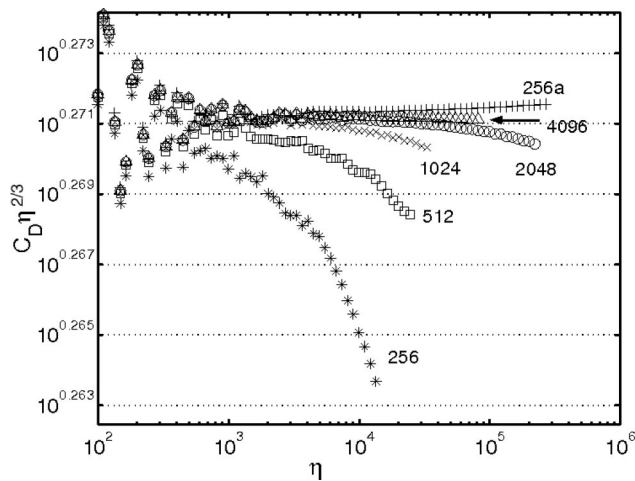


FIG. 21. The convergence of  $C_D \eta^{2/3}$  for the mesh sizes  $n=256, 512, 1024, 2048, 4096$ , shown starting from the bottom. The uppermost points (256a) are for  $n=256$  but with a higher (square-root) grid density at the tip.

running in Matlab 6 on a Sun Ultra-80, the code requires a few hours to compute solutions up to the value of  $\eta$  at which the solution can no longer be resolved, about  $10^5$  for this choice of  $n$ .

Once  $\bar{\theta}$  is known, we can obtain  $\Omega$  everywhere in the upper half disk using Eq. (21), and then compute the velocity and pressure field. Integrating Eq. (17) (for the Helmholtz flow) we obtain the physical location of all points in the upper half disk, including the shape of the free streamlines, which lie on the real diameter. Integrating the pressure jump along the fiber determines the drag.

In Fig. 21 we show the convergence of  $C_D \eta^{2/3}$  for the mesh sizes  $n=256, 512, 1024, 2048, 4096$ . Letting  $\eta_d$  be the value of  $\eta$  at which the drag deviates from the  $n=4096$  value by a specified factor, we estimate that  $\eta_d \sim n^3$ . This indicates that the minimum grid size needed to resolve the solution for a particular value of  $\eta$  scales as  $\eta^{1/3}$ . This happens to be the inverse length scale of the tip region, giving further evidence that the tip region controls the flow. In the same vein, Fig. 21 suggests that a 256-point grid with a square-root density of points near the tip is approximately as accurate as the  $n=2048$  uniform mesh. In addition to resolving the tip region, it may also be important to resolve the component of the next-order  $\eta^{-1}$  term with growing wave number  $2^{1/3} \eta^{2/3}$  in  $s$ , even as the term decays for large  $\eta$ .

The methods for the extended models are similar, except that the control parameters  $H$  and  $Q$  are used to determine the free variables  $I_0$ ,  $\gamma_B$ , and  $\gamma_F$  as part of the nonlinear solve (see Secs. VIA–VIC). In the wall-bounded cases, the desingularized  $\bar{\Omega}$  has a square-root behavior near the tip which precludes high accuracy of the computation (by contrast the Helmholtz  $\bar{\Omega}$  is apparently  $C^2$ , showing a  $k^{-3}$  decay of the Fourier components). This is dealt with by estimating numerically and then subtracting off the square-root behavior, and also using a square-root density of points at the tip for all parts of the computation except the FFT. The FFT is performed on a uniform but much finer grid with interpolated values. Thus a higher resolution of the tip is obtained at

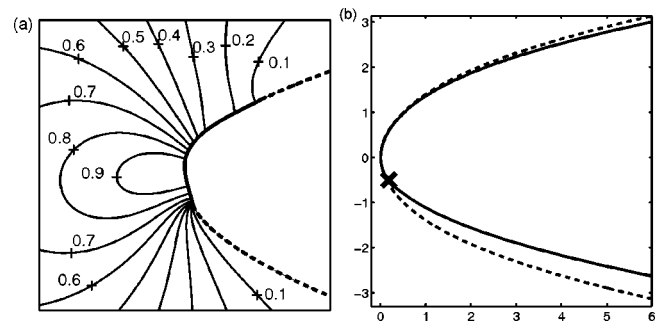


FIG. 22. (a) Contour plot of the pressure field for a fiber clamped at one-quarter length, perpendicular to the flow. (b) Solid line: The universal shape for fibers clamped at  $3/5$  length with an orientation of  $45^\circ$  to the oncoming flow. The clamp point is marked with an X. Dashed line: The symmetric universal shape, shown for comparison.

each step of the computation while the overall efficiency is maintained.

The solutions have been compared with symmetric and asymmetric flows past plates shown in the Appendix of Birkhoff *et al.*,<sup>17</sup> and with the sail solutions shown by Dugan.<sup>33</sup> In each of these cases agreement was obtained to the highest precision given by the previous results.

## APPENDIX B: ASYMMETRIC FIBER

With a simple modification to our Helmholtz-wake model (see Sec. V), obtained by allowing the argument of the stagnation point in the  $\zeta$ -plane to vary from  $\pi/2$  (see Hureau *et al.*<sup>41</sup>), one may compute asymmetric flows. We have used this method to compute the shape of a fiber clamped at any point along its length, held at any orientation relative to the free stream. We find the symmetric case to be representative of these cases as far as the asymptotic scaling of shape and drag. For cases in which the support point is closer to one end than the other, the two scaling regimes are separated by an intermediate interval in  $\eta$  in which the longer end exceeds the bending length but the shorter end does not. In Fig. 22(a) we show such a case, the fiber clamped at one-quarter length for  $\eta=10$ . In each of these cases of asymmetric clamping, the numerical solutions again show self-similar behavior when rescaled by the bending length, but now converge as  $\eta \rightarrow \infty$  to one of a two-parameter family of universal shapes, parametrized by clamp position and orientation. In Fig. 22(b) we show the universal shape for the clamp position at  $3/5$  length, with an orientation of  $45^\circ$  to the oncoming flow.

<sup>1</sup>M.A.R. Koehl, "When does morphology matter?" *Annu. Rev. Ecol. Syst.* **27**, 501 (1996).

<sup>2</sup>K.J. Niklas, "The influence of gravity and wind on land plant evolution," *Rev. Paleobot. Palyno.* **102**, 1 (1998).

<sup>3</sup>S. Vogel, *Life in Moving Fluids*, 2nd ed. (Princeton University Press, Princeton, 1994).

<sup>4</sup>M. Denny, B. Gaylord, B. Helmuth, and T. Daniel, "The menace of momentum: Dynamic forces on flexible organisms," *Limnol. Oceanogr.* **43**, 955 (1998).

<sup>5</sup>B. Gaylord and M.W. Denny, "Flow and flexibility. I. Effects of size, shape, and stiffness in determining wave forces on the stipitate kelps *Eisenia arborea* and *Pterygophora californica*," *J. Exp. Biol.* **200**, 3141 (1997).

<sup>6</sup>J. Zhang, S. Childress, A. Libchaber, and M.J. Shelley, "Flexible filaments

- in a flowing soap film as a model for one-dimensional flags in a two-dimensional wind," *Nature (London)* **408**, 835 (2000).
- <sup>7</sup>L.D. Zhu and C.S. Peskin, "Simulation of a flapping flexible filament in a flowing soap film by the immersed boundary method," *J. Comput. Phys.* **179**, 452 (2002).
- <sup>8</sup>G.I. Taylor, "On the shapes of parachutes," in *The Scientific Papers of Sir G.I. Taylor* (Cambridge University Press, Cambridge, 1963), Vol. 3, pp. 26–37.
- <sup>9</sup>A.D. Fitt and M.P. Pope, "The unsteady motion of two-dimensional flags with bending stiffness," *J. Eng. Math.* **40**, 227 (2001).
- <sup>10</sup>B. Thwaites, "The aerodynamic theory of sails. I. Two-dimensional sails," *Proc. R. Soc. London, Ser. A* **261**, 402 (1961).
- <sup>11</sup>Y. Couder, J.M. Chomaz, and M. Rabaud, "On the hydrodynamics of soap films," *Physica D* **37**, 384 (1989).
- <sup>12</sup>M. Gharib and P. Derango, "A liquid-film (soap film) tunnel to study two-dimensional laminar and turbulent shear flows," *Physica D* **37**, 406 (1989).
- <sup>13</sup>W.I. Goldburg, M.A. Rutgers, and X.-L. Wu, "Experiments on turbulence in soap films," *Physica A* **239**, 340 (1997).
- <sup>14</sup>M.A. Rutgers, X.-L. Wu and W.B. Daniel, "Conducting fluid dynamics experiments with vertically falling soap films," *Rev. Sci. Instrum.* **72**, 3025 (2001).
- <sup>15</sup>H. Helmholtz, "Über discontinuierliche Flüssigkeitsbewegungen," *Philos. Mag.* **36**, 337 (1868).
- <sup>16</sup>G. Kirchhoff, "Zur Theorie freier Flüssigkeitsstrahlen," *J. Reine Angew. Math.* **70**, 289 (1869).
- <sup>17</sup>G. Birkhoff and E.H. Zarantonello, *Jets, Wakes, and Cavities* (Academic, New York, 1957).
- <sup>18</sup>S. Balachandar, R. Mittal, and F.M. Najjar, "Properties of the mean recirculation region in the wakes of two-dimensional bluff bodies," *J. Fluid Mech.* **351**, 167 (1997).
- <sup>19</sup>T.Y. Wu, "Inviscid cavity and wake flows," in *Basic Developments in Fluid Dynamics*, edited by M. Holt (Academic, New York, 1968), Vol. 2.
- <sup>20</sup>G.K. Batchelor, "A proposal concerning laminar wakes behind bluff bodies at large Reynolds number," *J. Fluid Mech.* **1**, 388 (1956).
- <sup>21</sup>G.V. Parkinson and T. Jandali, "A wake source model for bluff body potential flow," *J. Fluid Mech.* **40**, 577 (1970).
- <sup>22</sup>F.T. Smith, "Laminar flow of an incompressible fluid past a bluff body: The separation, reattachment, eddy properties, and drag," *J. Fluid Mech.* **92**, 171 (1979).
- <sup>23</sup>K. Stewartson, "D'Alembert's paradox," *SIAM Rev.* **23**, 308 (1981).
- <sup>24</sup>M. Tanner, "Theories for base pressure in incompressible steady base flows," *Prog. Aerosp. Sci.* **34**, 423 (1998).
- <sup>25</sup>T.Y. Wu, "Cavity and wake flows," *Annu. Rev. Fluid Mech.* **4**, 243 (1972).
- <sup>26</sup>T.Y. Wu, A.K. Whitney, and C. Brennan, "Cavity-flow wall effects and correction rules," *J. Fluid Mech.* **49**, 223 (1971).
- <sup>27</sup>D. Riabouchinsky, "On steady fluid motion with free surfaces," *Proc. London Math. Soc.* **19**, 206 (1920).
- <sup>28</sup>S. Alben, M. Shelley, and J. Zhang, "Drag reduction through self-similar bending of a flexible body," *Nature (London)* **420**, 479 (2002).
- <sup>29</sup>J.M. Chomaz and B. Cathalau, "Soap films as two-dimensional classical fluids," *Phys. Rev. A* **41**, 2243 (1990).
- <sup>30</sup>L. Segel, *Mathematics Applied to Continuum Mechanics* (Macmillan, New York, 1977).
- <sup>31</sup>R.E. Goldstein and S.A. Langer, "Nonlinear dynamics of stiff polymers," *Phys. Rev. Lett.* **75**, 1094 (1995).
- <sup>32</sup>G.K. Batchelor, *An Introduction to Fluid Dynamics* (Cambridge University Press, New York, 1967).
- <sup>33</sup>J.P. Dugan, "A free-streamline model of the two-dimensional sail," *J. Fluid Mech.* **42**, 433 (1970).
- <sup>34</sup>O. Lorillu, R. Weber, and J. Hureau, "Numerical and experimental analysis of two-dimensional separated flows over a flexible sail," *J. Fluid Mech.* **466**, 319 (2002).
- <sup>35</sup>L. Ahlfors, *Complex Analysis*, 3rd ed. (McGraw-Hill, New York, 1979).
- <sup>36</sup>P.R. Garabedian and D.C. Spencer, "Extremal methods in cavitation flow," *J. Rat. Mech. Anal.* **1**, 367 (1952).
- <sup>37</sup>R. Estrada and R.P. Kanwal, *Singular Integral Equations* (Birkhauser, Boston, 2000).
- <sup>38</sup>G. Birkhoff, M. Plesset, and N. Simmons, "Wall effects in cavity flow," *Q. Appl. Math.* **8**, 151 (1950).
- <sup>39</sup>E. Wegert, *Nonlinear Boundary Value Problems for Holomorphic Functions and Singular Integral Equations* (Akademie Verlag, Berlin, 1992).
- <sup>40</sup>A.R. Elcrat and L.N. Trefethen, "Classical free-streamline flow over a polygonal obstacle," *J. Comput. Appl. Math.* **14**, 251 (1986).
- <sup>41</sup>J. Hureau, E. Brunon, and P. Legallais, "Ideal free streamline flow over a curved obstacle," *J. Comput. Appl. Math.* **72**, 193 (1996).
- <sup>42</sup>A. Ralston and P. Rabinowitz, *A First Course in Numerical Analysis* (Dover, New York, 2001).